UNIVERSITY OF OTTAWA

Coherent Anti-Stokes Raman Scattering Microscopy for Biomedical Applications

By

Huda Yousif

Thesis submitted in partial fulfillment of the requirements for the
Master of Applied Science degree in Biomedical Engineering

School of Electrical Engineering and Computer Science
University of Ottawa
The Ottawa-Carleton Institute for Biomedical Engineering

Abstract

Coherent anti-Stokes Raman scattering (CARS) microscopy is considered as a powerful tool for non-invasive chemical imaging of biological samples. CARS microscopy provides an endogenous contrast mechanism that it is sensitive to molecular vibrations. CARS microscopy is recognized as a great imaging system, especially in vivo experiments since it eliminates the need for the contrast agents.

In this thesis, CARS microscopy/spectroscopy is built from scratch by employing a single (Ti-Sapphire) laser source generating 65 femtosecond laser pulses centered at 800 nm wavelength. Two closely lying zero dispersion photonic crystal fiber (PCF) is used to generate the supercontinuum for the Stokes beam to generate CARS at 2885 cm^{-1} to match lipids rich vibrational frequency. XY galvanometers are used for laser raster scanning across the sample. The initial generation of CARS signal was in the forward direction. After guaranteeing a strong CARS signal, images for chemical and biological samples were taken. To achieve a multimodal imaging technique, CARS microscopy imaging system is combined with two- photon excitation fluorescent (TPEF) and second harmonic generation (SHG) imaging techniques, where various information was extracted from the imaged samples. Images with our CARS microscopy show a good resolution and sensitivity.

The second part of my work is to reduce the footprint for this setup to make it more suitable for use in clinical applications. For that reason, I integrated a homebuilt endoscope and all fiber femtosecond laser source together to get a fiber based imaging system. Proof of principal for the integrated system is achieved by obtaining a reasonable agreement in accuracy and resolution to those obtained by the endoscope driven by Ti-sapphire laser.

Acknowledgement

I would like to express my appreciation to my supervisor, Dr. Hanan Anis, who accepted me into her research group in 2012. She has taught me to have confidence and be patient in my research and work. Professor Anis supported my contribution in events such as workshops, conferences, and courses to expand the depth of my knowledge. Professor Anis has helped me to see the big picture and keep my goals in mind, and focusing on trying to solve problems.

I must extend my thanks to my colleagues at the Photonics lab at the University of Ottawa. First, I would like to thank Majid Naji for spending hours helping me in the lab when I started to understand the functioning of the first CARS setup, and for helping in operating the laser scanning system for the new setup. I would also like to thank Brett Smith for explaining the CARS endoscopy imaging system and how to work. I would like to thank Hussein Kotb for his strong support in laser measurements and characterization, and in integrating the femtosecond fiber laser with the nonlinear endoscope. I also thank Mohammed Abdelalim for his guidance, motivation, and fruitful discussions. I would like also to thank Robert Hunter for his support during my thesis writing, and assisting in image processing.

I also want to thank the other researchers I have worked along-side in the lab over the past years who have encouraged me and created an enthusiastic work environment.

Finally, I must thank my family, especially my husband and children who have encouraged me, supported me throughout my degree.

Statement of Originality

The author declares that the results presented in this thesis were obtained during the course of her M.A.Sc. research under Dr. Hanan Anis, and that this is, to the best of her knowledge, original work.

Table of Contents

List of Figures

List of symbols

NIR Near-infrared

SHG Second harmonic generation

CARS Coherent Anti-Stokes Raman Scattering

CW Continuous wave

NA Numerical aperture

PCF Photonic crystal fibre

ZDW Zero-dispersion wavelength

TPEF Two-photon excitation fluorescence

SFG Sum frequency generation

THG Third harmonic generation

SRS Stimulated Raman Scattering

UV Ultraviolet

IR Infrared

SC Supercontinuuum

SPM Self-phase modulation

FWM Four-wave mixing

GDD Group delay dispersion

GVD Group velocity dispersion

OSA Optical spectrum analyzer

SPD Spectral power density

PMT Photomultiplier tube

TTL Transistor-transistor logic

USAF United States air force

ECM extracellular matrix

NI National Instrument

DAQ Data acquisition

PBG Photonics bandgap

FWHM Full width at half maximum

FPGA Field-programmable gate array

MFD Mode field diameter

Chapter 1 : Introduction to Nonlinear Imaging

1.1 Introduction

Optical microscopy is an excellent imaging modality, capable of probing living tissue and visualizing morphological details that cannot be resolved by other modalities, such as ultrasound and magnetic resonance imaging (MRI) [1]. However, optical microscopy typically lacks chemical specificity, and in many cases requires labeling. For example, the contrast in confocal microscopy is based on refractive index differences, and is unable to probe the chemical composition of specimen structures [2]. The fluorescence labeling technique is also invasive, as it requires introducing a fluorescent dye into a cell, or genetically modifying a cell to express a fluorescent protein to image the region of interest.

In contrast, Raman microscopy provides chemical selectivity, and does not require dyes or sample labeling. The Raman Effect is an inelastic scattering of a photon by molecules that are excited to a higher vibrational level; a portion of the photon's energy is absorbed by a bond, thereby scattering it with a longer wavelength. This wavelength shift depends on the nature of the bond the photon interacts with, and the spectrum of Raman shifted photons yields specific chemical information. Raman microscopy has many biomedical applications, and it also has limitations. Its signal is extremely weak, which means it requires higher laser power, longer acquisition times and extended integration periods of 100 ms to 1 s per pixel. These drawbacks

can damage biological specimens, which restricts using Raman microscopy for studying living samples [3].

This thesis focuses on the use of Coherent Anti-Stokes Raman Scattering (CARS). CARS has many advantages such as:

(a) Coherence: CARS is a nonlinear optical process that employs two laser beams (pump and Stokes) to generate a coherent optical signal. As a result, the CARS signal is orders of magnitude higher than spontaneous Raman microscopy, thereby allowing video-rate vibrational imaging.

(b) Label free: CARS is sensitive to the vibrational contrast of the sample. When the frequency difference of the beams matches the frequency of the Raman molecular vibration of the material, it generates an anti-Stokes signal, therefore, there is no need for specimen labeling/staining. CARS signal provides contrast, as it is generated when the frequency difference of the applied laser matches the specimen vibrational frequency.

(c) 3D sectioning capabilities: Due to the nonlinear nature of the CARS process, the CARS signal is only generated at the focal volume providing inherent 3D sectioning capability. In contrast, confocal microscope requires the use of pin holes which wastes a lot of power and result in photobleaching.

(d) Deep penetration: CARS allows for deep penetration because the laser sources used are at the near infrared region (NIR). Thus, there will be less light scattering and light absorption inside the sample.

CARS microscopy is particularly useful in the detection of high lipid content. As a result, it was applied to many clinical applications such as tracking lipid droplet metabolism, myelinated axon structure, spinal cord demyelination, cardiovascular disease, and determination of hepatic fat content of liver tissue [1] [4]. However, the significant costs for equipment and the need for highly qualified personnel have limited its entry into mainstream medicine. Figure 1.1 shows the

image of an atherosclerotic plaque deposition in a human artery wall obtained by Chemnitz et al., highlighting the significance of a multimodal, nonlinear microscope [5].

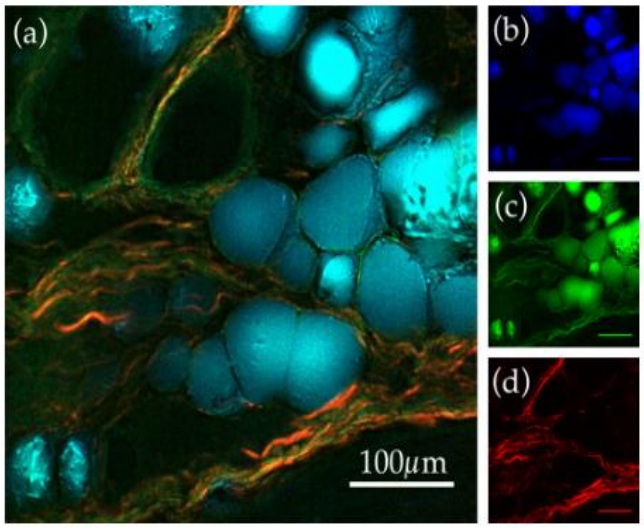

Figure 1-1 Multimodal nonlinear microscopic image of an atherosclerotic plaque deposition in a human artery wall. The combined CARS microscopic images acquired at the aliphatic methylene stretching vibration at 2845 cm−1 (blue) and the methyl stretching vibration at 2845 cm^{-1} (blue) and the methyl stretching vibration at 2930 cm^{-1} (green) for imaging the lipid and protein distribution are contrasted to the combined TPEF and SHG signal of collagen and elastin (red) [5]

Detailed explanations on how these modalities are generated and exploited are presented in the following chapters.

1.2 Historical background of CARS

CARS was first reported by Marker and Terhune [6]. They used a giant pulsed ruby laser to investigate the third order response of different materials. Figure 1.2 shows the experimental set up for the first CARS spectroscopy. They called this technique three wave mixing.

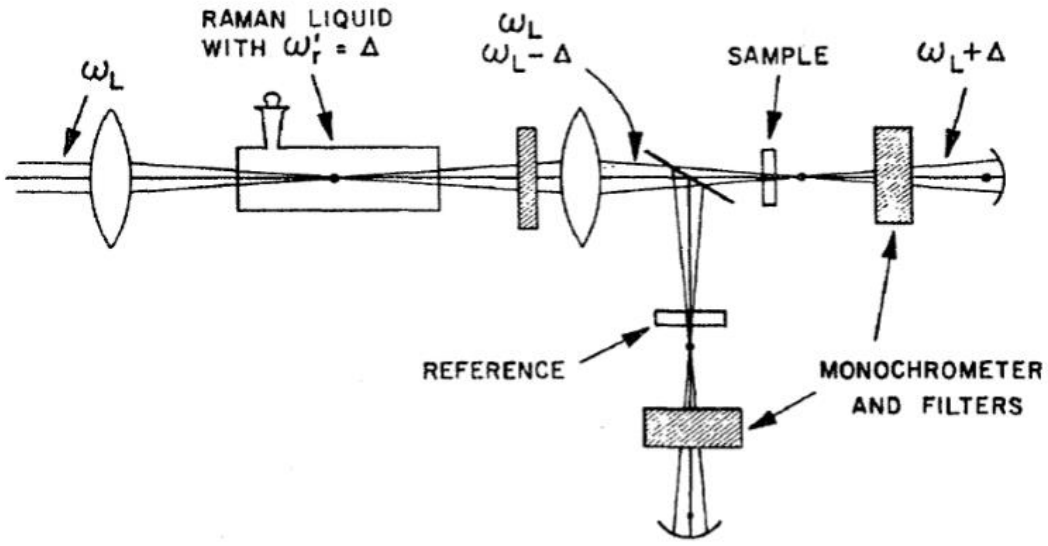

Figure 1-2 Schematic diagram of first CARS spectroscopy experimental setup [6]

A decade later, Begely et al. evaluated this technique, and renamed it the Coherent Anti-Stokes Raman Spectroscopy spectroscopic tool. They showed that a signal obtained with this technique is about 10^5 stronger than with spontaneous Raman scattering, and that it uses significantly less applied power (1-2 mW compared to 1 W). It also increases the rejection of most of the background fluorescence by approximately nine orders of magnitude [7]. From then on, CARS spectroscopy became an important tool for investigating biological compounds when background fluorescence was a problem with conventional spontaneous Raman scattering. CARS also used to analyze gases and measure the nonlinear properties of solids and liquids.

In 1982, Duncan et al. presented the first CARS microscope that used two synchronously pumped CW mode-locked dye lasers with non-collinear beam geometry in the phase matching direction to image the distribution of distinct chemical species in a microscopic sample region, as shown in Figure 1.3 [8]. Images of onion skin cells in D_2O were obtained using a CARS signal produced in the 2450 cm^{-1} band. However, the non-collinear beam geometry they

employed degraded the image quality, and using a light source in the visible region resulted in large non-resonant backgrounds that disturbed the vibrational contrast.

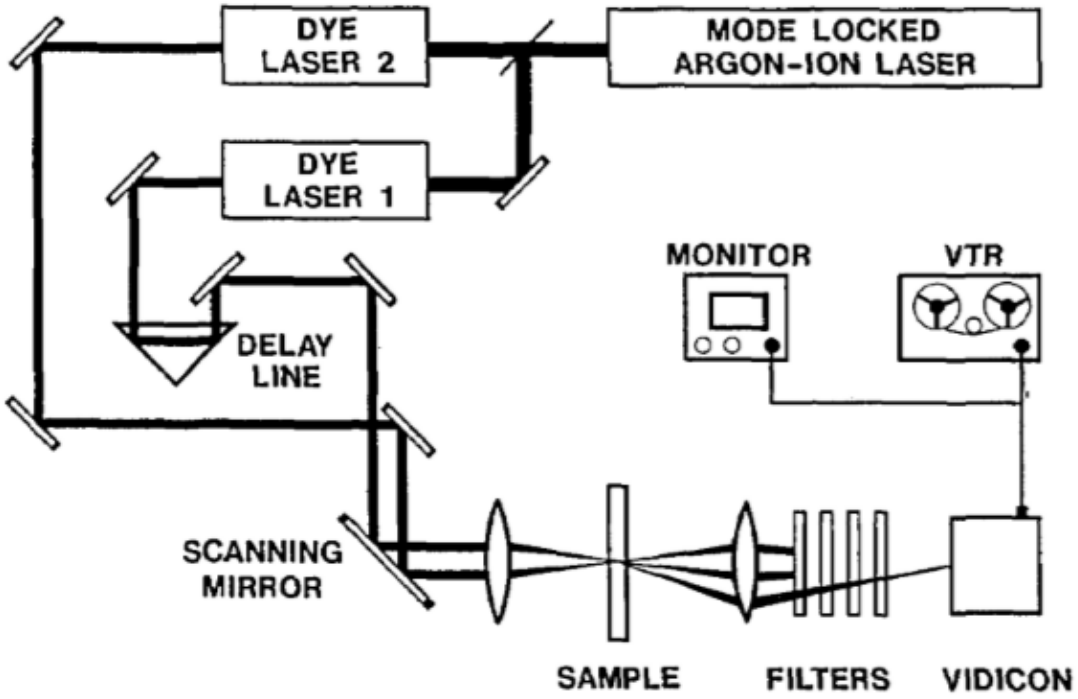

Figure 1-3 Shows the schematic drawing of first CARS microscope constructed by Duncan et al. [7]

Few developments addressed these technical problems until 1999, when Zumbusch et al. renewed interest in CARS microscopy [9]. Their setup used near-infrared laser beams to demonstrate vibrational imaging of chemical and biological samples, and obtained high spatial resolution, sensitivity and three-dimensional sectioning. They used light sources at the near infrared region to reduce the non-resonant background, and an objective lens with a high numerical aperture (NA) to focus the beam tightly. These modifications reduced the phase-matching conditions, rejected the background signal, decreased sample photodamage and increased the opportunities for three-dimensional optical sectioning at different focal planes.

In 2001, Cheng et al. reported using CARS microscope with two synchronized picosecond pulse trains. This approach increased spectral resolution and sensitivity for three-dimensional vibrational imaging of living cells [10].

One of the major obstacles of using CARS microscopy is its expense, as two synchronized solid-state lasers are required to drive the microscope. Murugkar et al., addressed this issue by developing a CARS microscope system that needed only a single laser source to produce the pump and Stokes beams. Photonic crystal fiber (PCF) was used to generate a supercontinuum, which produced the second beam (Stokes) [11]. The PCF had custom dispersive properties, particularly at two close lying zero-dispersion wavelengths. An 800 nm light was focused on the PCF to generate broad-spectrum output with the blue and red light shifted, and this produced a supercontinuum with a peak of 1040 nm, which was adequate to use as a Stokes beam. This resulted in the chemically specific image for adipocyte cells, as shown in figure 1.4.

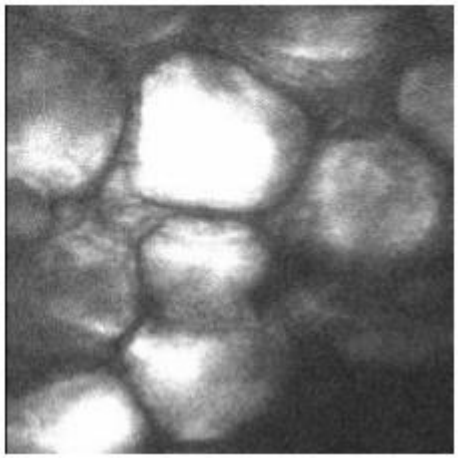

Figure 1-4 Image of adipocyte cells at a depth of 100 µm in a mouse ear imaged in the forward mode through several hundred microns of tissue [10]

Real-time in-vivo CARS imaging is the ultimate goal, and what motivated researchers [12] [13] [14] to develop a compact, nonlinear optical endoscope. Reducing the size of the laser sources is another major step toward achieving a compact multimodal nonlinear imaging system that can

be used at a patient's bedside. Kotb et al. developed a femtosecond fiber laser with a center wavelength of 1030 nm, which could be integrated with a home built miniaturized nonlinear endoscope.

1.3 Thesis Objectives

Given our labs effort in developing a single source microscope and endoscope, it was natural to combine the miniaturized nonlinear endoscope built by graduate student Brett Smith with the femtosecond fiber laser developed by Ph.D. student Hussein Kotb goal was to apply this setup to in-vivo bio-imaging.

While working on integrating the femtosecond fiber laser with the nonlinear endoscope, we had to move the setup to a new lab. This meant that I had to disassemble our CARS spectroscopy/ microscopy system, then build another setup in the new photonics lab and demonstrate its biomedical applications. Due to the inherent complexity of CARS microscopes this was a not a trivial task, but it did give me the opportunity to develop skills I did not possess before starting this research. This included pulse compression using a prism compressor, using the autocorrelator to measure pulse width, launching a compressed pulse into a PCF with 40% coupling efficiency to generate the supercontinuum, and precise optical alignment to make the pump and Stokes beams, overlap spatially. Consequently, the focus of my thesis shifted to redevelopment of the CARS microscope, and making the improvements necessary to apply the system to biomedical applications.

1.4 Thesis Outline

Chapter 2 provides a summary of nonlinear processes and microscopy, and an overview of CARS microscopy. It also addresses the multiphoton and second harmonic generation processes, and focuses on understanding the fundamental CARS process.

Chapter 3 describes the home built CARS spectroscopy and microscopy setup, and provides the results obtained with CARS spectroscopy and imaging using CARS microscopy.

Chapter 4 presents and describes the imaging results of the integration of our home built femtosecond fiber laser with our, also home built, endoscope, and discusses a compact nonlinear optical microscope for bedside medical imaging applications.

Chapter five provides the conclusions drawn from the work in this thesis, and summarises potential future applications.

1.5 Personal contribution

After I was accepted as a graduate student at the University of Ottawa and joined professor Anis group, it was the time to move from our old lab to new lab, advanced research complex ARC building. I disassembled and re-assembled the CARS setup. I also designed the prism compressor that is required to compress the pulse so that the pulse can efficiently coupled to the PCF. Moreover, I fully characterized the laser at each point in the setup to ensure that I have the precise characteristics needed to generate CARS signal. For image reconstruction, I interfaced a LABVIEW based microscope scanning program with the XY scanning mirrors. I tested the CARS spectroscopy and microscopy on chemical microspheres samples and mouse fat cells as biological samples. I prepared the chemical samples and I sourced the biological samples, prepared them for imaging. In addition to CARS microscopy, I performed two photon excitation

florescence and second harmonic generation microscopy for biological samples. For the integration of femtosecond fiber laser with miniaturized nonlinear endoscope part, it was a group effort. A team from our lab developed the femtosecond fiber laser at wavelength 1030 nm. While another team in our lab built the nonlinear endoscope. My contribution was to combine those two devices and test it by performing a two-photon excitation fluorescent (TPEF) imaging with chemical and biological samples and compared the images with images were taken with golden standard imaging microscopes, to make a compact, portable, and cheap nonlinear imaging system.

Chapter 2 : Nonlinear Optical Microscopy

2.1 Introduction

This chapter begins with a brief description of different nonlinear processes (Section 2.2). This is followed by a discussion of nonlinear microscopy (Section 2.3), and investigation of some nonlinear modalities, including CARS, two- photon excitation fluorescent (TPEF) and second harmonic generation (SHG). A key element of these modalities is the use of a single femtosecond laser source operating at 800 nm combined with a PCF to produce a supercontinuum from white light. A 1040 nm Stokes beam is selected which, when combined with the pump beam, will generate the anti-Stokes beam for the CARS process. The final nonlinear effect discussed in this chapter is supercontinuum generation.

2.2 Nonlinear Optical Processes

Nonlinear optics describes the behaviour of light in a nonlinear media, which occurs when the material system responds nonlinearly to an applied electric field. The nonlinearity is observed only at high light intensities [15]. Nonlinear processes can be depicted by energy level diagrams such as Figure 2-1, which illustrates the nonlinear energy level process for TPE, SHG, CARS and Stimulated Raman Scattering SRS.

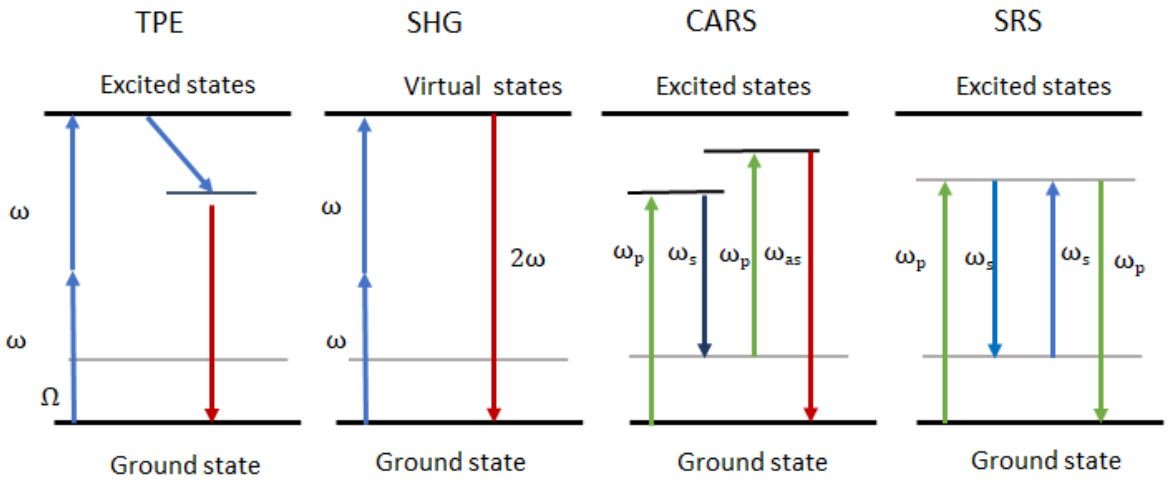

Figure 2-1 Energy level diagram for TPE, SHG, CARS and stimulated Raman Scattering SRS

Figure 2-1 shows the energy levels of the interaction of multiple photons with the electronic and vibrational energy levels of a molecule. In the TPE process, the molecule absorbs two photons and is excited to a higher electronic state; when it relaxes to a lower vibrational level it emits a lower energy photon. With SHG, two photons are instantaneously up-converted to a single photon with twice the energy. In the CARS process, a four-wave mixing process generates a new field at the anti-Stokes frequency $\omega_{as} = 2\omega_p - \omega_s$. When the frequency difference of $\omega_p - \omega_s$ matches the molecular vibration of the sample, the nonlinear response is resonant [15]. With SRS, pump and Stokes frequencies are incident on the sample; if the frequency difference $\omega_p - \omega_S$ matches a molecular vibration of the sample, a stimulated excitation of vibration transitions occurs. The intensity of the pump field decreases and that of the Stokes field increases [16] [17].

Figure 2-1 shows how SHG and CARS are parametric processes; that is, optical processes between the light and the material in which the quantum state of the material is unchanged, and energy transfer from the light to the material does not occur. TPEF and SRS are examples of non-parametric processes. The main difference between parametric and nonparametric processes is that the photon energy is always conserved in a parametric process, whereas a nonparametric process transfers the photon energy to or from the material medium [15].

2.3 Nonlinear Optical Microscopy

Nonlinear optical microscopy has many advantages over standard linear microscopy, including the use of Near Infrared light (NIR), region between 800-1000 nm,that provides greater depth penetration than infrared microscopy techniques, [18]. In addition, tissue photo-damage when using NIR radiation is less than that of visible, region 400-700 nm radiation, as the two-photon excitation process occurs at the local focal point, which minimizes tissue damage in other areas [18].

When an NIR laser beam is tightly focused, there is localized nonlinear interaction only at the focal point, while the out of focus areas remains inactive, as shown in figure 2-2 (a). Conversely, Figure 2-2(b) illustrates how single-photon excitation results in high excitation volume [19].

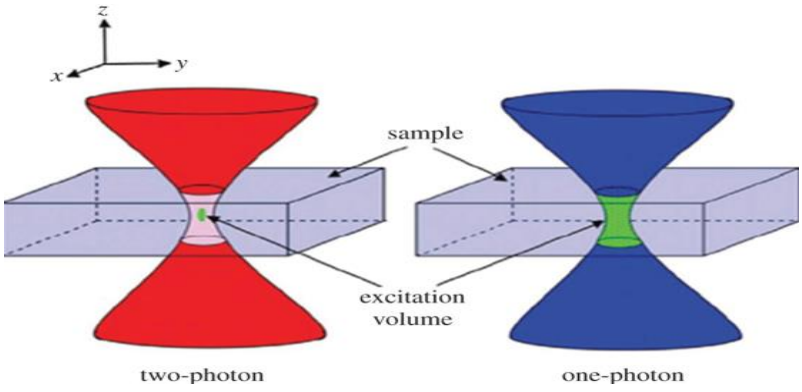

(a) *(b)*

Figure 2-2 shows the difference between a) two-photon interaction volume, and b) single–photon interaction volume [19]

Localization of the excitation volume in multiphoton microscopy techniques provides several benefits, the most important of which is that the three-dimensional resolution of a two-photon excitation microscope is close to what can be achieved with a confocal microscope, without using pin-holes or wasting laser power. Moreover, photo-bleaching (loss of color by a pigment when the sample is illuminated) is minimized.

The main disadvantage of nonlinear microscopy is the need for high power, ultra-short laser sources, which are often complicated and very expensive. Femtosecond fiber lasers are becoming more popular, and integrating them with nonlinear microscopy could greatly reduce the cost, space and complexity.

2.3.1 Second-order nonlinear process: Second Harmonic Generation (SHG)

Second Harmonic Generation (SHG) is a second-order nonlinear optical process in which two photons at frequency ω interact with non-centrosymmetrical medium, and combine to form a new photon with twice the energy and double the frequency (2ω) of the initial photons. Figure

2.3 shows how two photons of frequency ω are absorbed and a photon of frequency 2ω is simultaneously created in a single quantum mechanical process. The solid horizontal line in the Figure 2-3 (b) represents the atomic ground state, and the dashed lines represent the virtual levels.

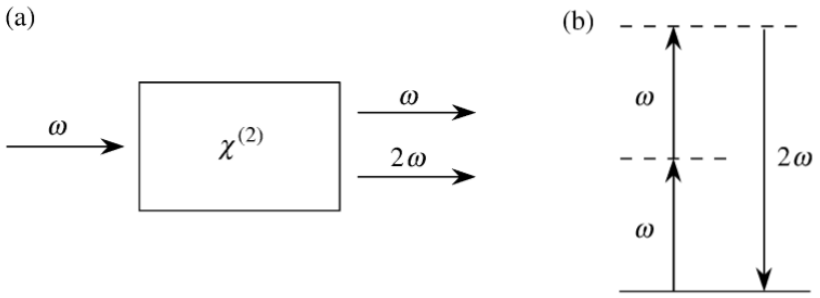

Figure 2-3 shows a) the block diagram of second-harmonic generation and b) the energy-level diagram for the second-harmonic generation [15]

To further understand the SHG process, we look at the resulting polarization when a material with second-order susceptibility $\chi^{(2)}$ is exposed to a laser beam with an electric field strength of:

$$\tilde{E}(t) = Ee^{-\omega t} + c.c \tag{2.1}$$

Where c.c is the complex conjugate. The polarization created in a non-centrosymmetric medium is given by:

$$P_2(t) = 2\epsilon_0\chi^{(2)}EE^* + \left(\epsilon_0\chi^{(2)}E^2e^{-i2\omega t} + c.c\right) \tag{2.2}$$

Equation 2.2 shows that the$P_2(t)$, second order polarization consists of a contribution at zero frequency (the first term), and a contribution at frequency 2ω (the second term). *E* is the scaler quantity of the applied electrical field, *m* is the electron rest mass. The first contribution does not generate electromagnetic radiation, as its second-time derivative vanishes. Instead, it causes an

optical rectification that creates a static electric field across the nonlinear material. The second contribution can generate radiation at the second-harmonic frequency.

SHG microscopy was first introduced by Shepard et al. in 1977 [20], was considered a contrast microscopy mechanism. Figure 3.20 illustrates the first harmonic microscope. Roth et al. pioneered applying SHG-based microscopy to biological samples, imaging a rat-tail tendon in 1980 [21].

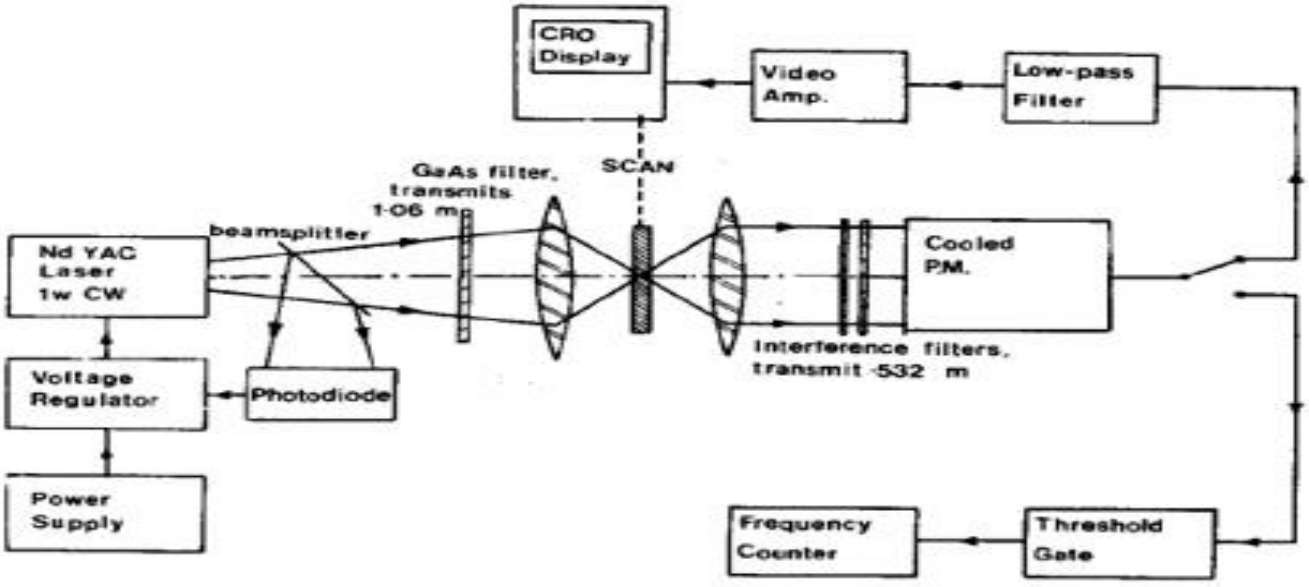

Figure 2-4 The first harmonic microscope [20]

However, researchers began to use it to image biological samples, such as collagen in mouse tendon tail [21], or biomolecular arrays in biological samples [22]. The contrast in SHG microscopy from tissues is produced from endogenous species, and no labeling is required.

Biological materials that assemble into ordered non-centrosymmetric structures, such as collagen, mitotic spindles, act-myosin complexes and microtubules, are known to generate SHG [22], which can reveal more structural information about collagen in tissues than is possible with other microscopy techniques [23]. For example, collagen in the extracellular matrix (ECM) in ovary tissue is substantially transformed in cancer, connective tissue diseases, autoimmune disorders and cardiovascular diseases. Moreover, since the laser excitation wavelengths are typically in the NIR spectral range (700–1000 nm), SHG microscopy can achieve high-resolution imaging to hundreds of microns.

2.3.2 Third-order nonlinear process

Third-order nonlinear processes include two-photon Excitation Fluorescence, third harmonic generation, SRS and CARS. In the following section, we focus our discussion on the mechanics behind the generation of TPEF and CARS processes.

2.3.2.1 Two-Photon Excitation Fluorescence process

TPEF was firstly demonstrated by Kaiser and Garrett in 1961 [24] , and Helmchen et al. presented the potential of TPEF in microscopy in 1990 [25]. Since then, TPEF microscopy has become a standard technique for imaging biological samples.

TPEF is a third-order nonlinear process that involves two-photon excitation, followed by a fluorescence emission. TPEF has many advantages over single-photon fluorescence, which stimulates an atomic transition, since with TPEF the energy of two photons is absorbed simultaneously. A single photon process requires a photon in either the ultraviolet spectrum or the blue/green region, while TPEF only needs low-frequency photons (typically in the infrared spectral range) to promote electrons to a real excited state. A single photon of the same

frequency does not have the energy required to bridge the band gap. Two-photon absorption is also useful if the excited state is not connected to the ground state in a single photon absorption transition. As this transition involves a real state, it is a nonparametric process in which lifetimes are long enough for some vibrational energy transfer before it decays back to the ground state. Figure 2-6 shows the TPEF energy diagram.

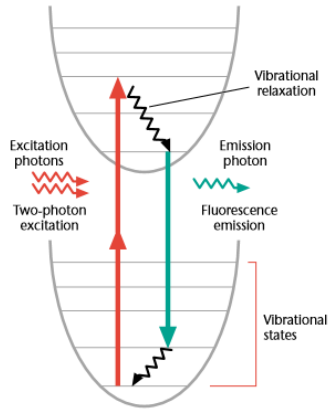

Figure 2-5 Shows the TPEF process energy diagram [26]

The generated photons are blue shifted with respect to the exciting photons, which has a longer wavelength, so it is quite easy to separate them spectrally. With single photon fluorescence microscopy, separating the excitation and emission wavelengths can be problematic. As the energy difference between the two frequency bands is relatively small, filter selection can be delicate. Figure 2-4 illustrates the difference between the one-photon (upper image) and two-photon (lower image) with respect to emission photons.

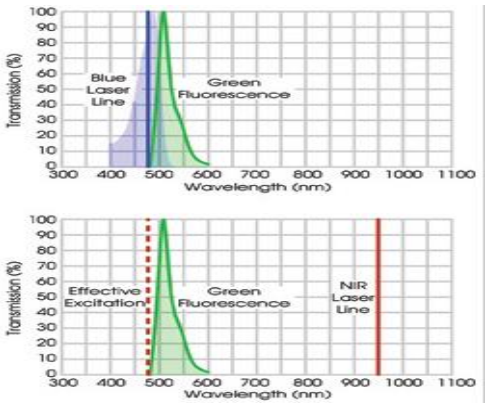

Figure 2-6 The difference between one-photon (upper image) and two-photon (lower image) microscopy with respect to emission photons [27]

Many biomedical applications [8] [1], have benefited from combining the TPEF and SHG nonlinear processes. A laser at frequency ω yields an SHG signal of 2ω, and the corresponding TPEF signal is red-shifted due to the internal conversion processes in the fluorophore. Thus, both signals are easily separated spectrally.

2.3.2.2 Coherent Anti- Stokes Raman Scattering (CARS)

CARS is a third order nonlinear process in which pump and Stokes beams with center frequencies of ω_p and ω_s, respectively, stimulate a sample through a wave-mixing process. The pump field *Ep* (ω_p) and Stokes field E_s (ω_s) interact with the sample and generate an anti-Stokes field E_{as} at the frequency $\omega_{as} = 2\omega_p - \omega_s$, by:

$$\chi_F^{(3)}\left(\omega_{as} = \omega_p - \omega_s + \omega_p\right) = \frac{-\left(\frac{\epsilon_0 N}{6m\omega_v}\right)\left(\frac{\partial\alpha}{\partial q}\right)_0^2}{[(\omega_p - \omega_s) - \omega_v] + i\gamma} \qquad (2.3)$$

Where ω_{as} is the anti-Stokes generated frequency, N is the number density of molecules, $(\partial\alpha/\partial q)$ is the change of polarizability of a molecule with respect to the internal precise distance, ω_v is the inherent resonant molecular frequency and γ is the relaxation rate. A nonlinear response occurs in the system when $\omega_p - \omega_s$ is equal to the molecular resonant frequency ω_v**.** Therefore CARS is useful as a diagnostic tool to determine the presence of chemical species by their Raman vibrational modes. CARS can differentiate between regions that contain the molecule being probed and those where it is absent, as the laser scans from one region to the other. The energy diagram of CARS is shown in Figure 2-7. It indicates that CARS is a four-wave mixing process with a new field at the anti-Stokes frequency $\omega_{as} = 2\omega_p - \omega_s$. When the energy difference between ω_p and ω_s matches the molecular vibration of the sample, the scattering process is resonantly enhanced.

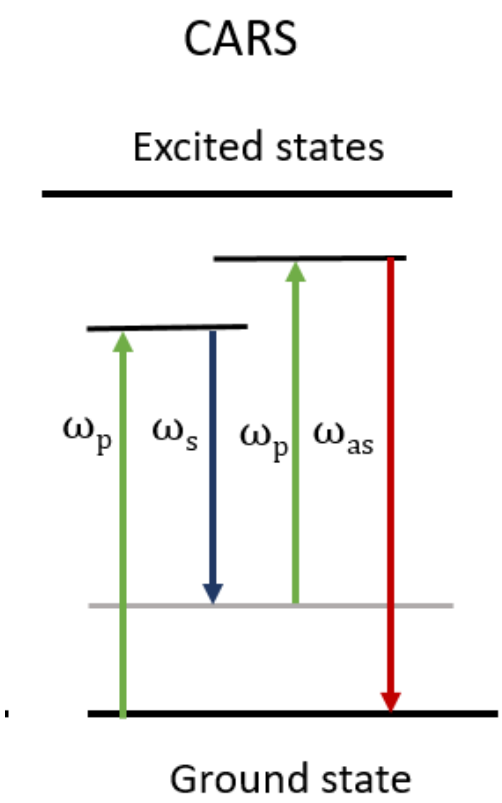

Figure 2-7 CARS energy level diagram

CARS microscopy has been used to visualize living cells with different vibrational contrast modes, such as amide I vibration (protein) [28], and the C-H (carbon-hydrogen) group of stretching vibrations (lipids) [11] [29]. Lipids with a CH vibration mode have a high signal that single phospholipid bilayers can visualize [3] [10]. Lipids are rich in CH_2 group, and have a strong band in the Raman spectrum at 2845 cm^{-1}, which is attributed to the symmetric stretching mode of the CH_2 band. By tuning the laser frequency difference of ω_p- ω_s to 2845 cm^{-1}, the laser illuminates the lipids in the sample and generates a strong CARS signal. Lipids act as a structural component of the cell membrane, and as they are a smaller molecule than protein or DNA, their structure and functionality changes if dye or fluorophores are added to the cell for

imaging purposes. Therefore, CARS is an appropriate imaging method, since it is a non-invasive, label and dye free technique to visualize lipids in rich biological samples.

There are several main considerations when choosing the pump and Stokes wavelength. First, most biological samples contain a significant amount of water, so it is important to use wavelengths in the NIR where water absorption is minimal. Figure 2.8 illustrates that the best laser wavelength to minimize the effects of water absorption is below 1350 nm. There is also a lower limit for pump and Stokes wavelength selection, if scattering is to be minimized. As the Rayleigh scattering cross section is proportional to λ^{-4}, the scattering effect will be minimized for longer wavelengths. Therefore, with respect to optimal wavelengths, the best compromise between these two considerations is to use pump and Stokes wavelengths in the range of 800 nm to 1100 nm.

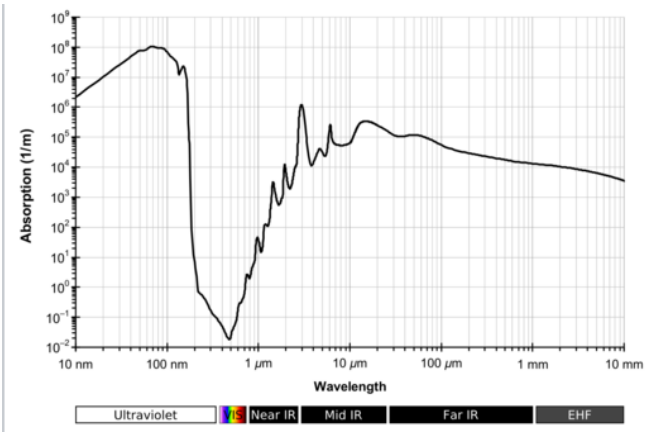

Figure 2-8 Absorption coefficient of water in the visible and IR region [29]

Since the CARS signal is proportional to the square of the incident laser light intensity, pulsed lasers are the best choice as they have the highest peak powers, and maximum generated CARS signals. Thus, choosing the laser pulse width must be done with careful consideration. However,

even with high peak laser power, it can still cause an increase in generating non-resonant CARS background. This is due to the wide spectrum of femtosecond laser pulses (~ 150 cm^{-1}), which is much larger than the probing Raman line width of ~10-20 cm^{-1}. The femtosecond laser uses a small segment of its spectral components to pump the narrow Raman line, which will generate a large non-resonant background signal that often blurs chemically specific contrast. The only way to decrease the laser pulse bandwidth is to increase the pulse width. Though this will decrease the laser peak power, it will also reduce non-resonant background.

2.3.2.3 Supercontinuum generation

We now discuss supercontinuum (SC) generation, as it will be used to produce the Stokes beam for the CARS signal. The supercontinuum is key to use a single laser source for our CARS microscopy.

SC generation occurs when an ultrashort laser interacts with a nonlinear material to form broad continuous spectra. Alfano and Shapiro first reported supercontinuum generation from a body of BK7 glass [30]. They propagated a 5mJ picosecond laser at a 530 nm wavelength to generate a white light spectrum covering a visible range of 400 to 700 nm [30] [31].

Figure 2-9 illustrates an example of supercontinuum generation using two close to zero dispersion wavelengths, by changing the laser wavelength [11].

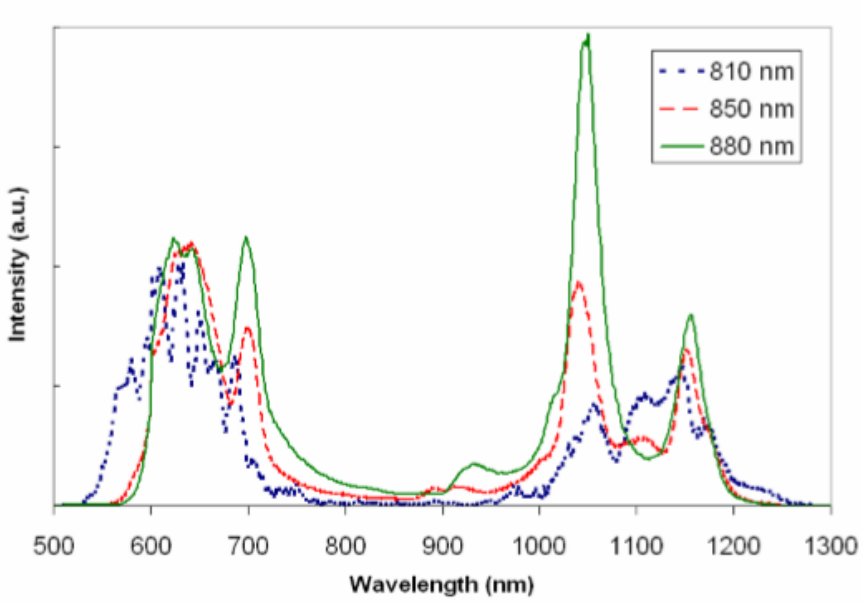

Figure 2-9 The generated supercontinuum after propagating the pump source through the two closely zeros dispersion wavelengths PCF [11]

The process of supercontinuum generation for the two closely lying zero dispersion wavelengths used in this thesis is explained as follows: SPM is the dominant mechanism for spectrum broadening, since it provides the seed wavelengths for four-wave mixing (FWM). In the absence of soliton fission in a PCF with two closely lying ZDWs, the SC has far less noise compared to SC from conventional PCFs with one ZDW [11].

2.4 Conclusion

This chapter presented an overview of various nonlinear optical processes, including second order (SHG) and third order (CARS and TPEF), and the energy level diagrams of the two processes. The benefits of using different techniques of nonlinear optical microscopy are also discussed.

Chapter 3 : Experimental setup and results

3.1 Introduction

This chapter focuses on the experimental set-up for our multimodal non-linear microscope, with Section 3.2 highlighting the building of the CARS setup and the components needed. Section 3.3 details the spectroscopy and microscopy of nonlinear techniques, and the imaging results of florescent beads, polystyrene and biological samples.

3.2 CARS microscopy experimental setup

The CARS setup consists of five main elements: the laser source, supercontinuum PCF to generate the Stokes beam, a laser scanning system, optical design, data acquisition and a detection source. Each of those elements is described in the following subsections. The CARS optical set-up and scanning system block diagram is shown in Figure 3-1.

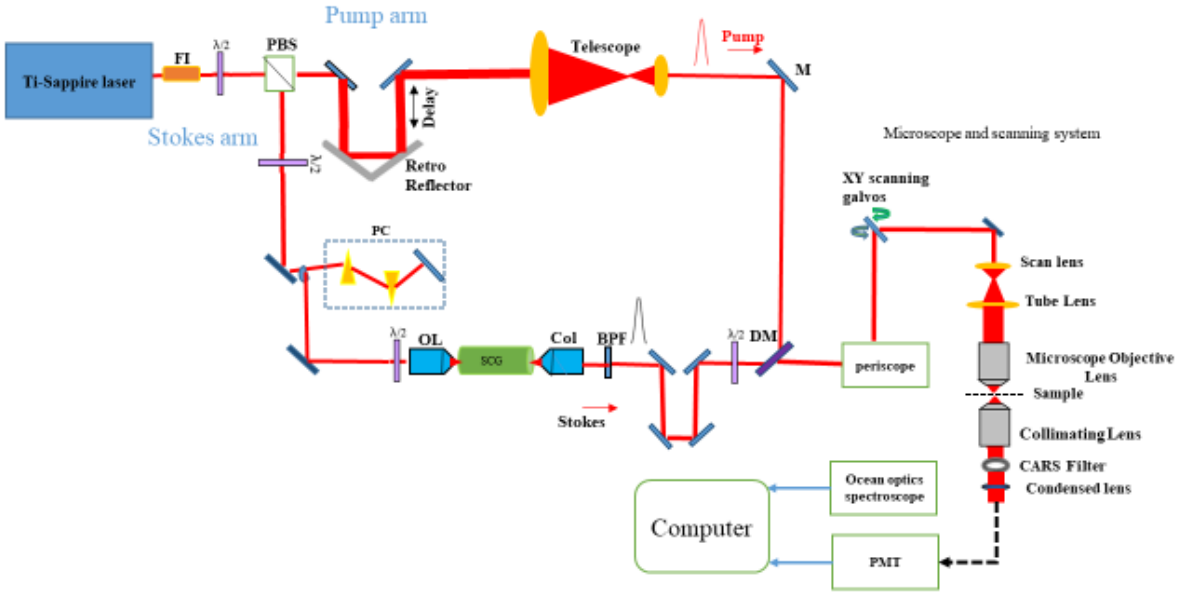

Figure 3-1CARS optical set-up and scanning system block diagram. Legend of optical elements: FI: Faraday Isolator, λ/2: Half-wave plate, PBS: Polarized beam splitter, M: Mirror, PC: Pulse compressor, OL: Objective lens, SCG: Supercontinuum generation, Col: collimating objective lens,BPF: Band pass filter DM: dichroic mirror, PMT: Photonmultiplier tube

3.2.1 Laser source

The laser source depicted in Figure 3-1 is a Ti: Sapphire (Spectra -Physics) generating 65 fs laser pulses at an 80 MHz repetition rate. The laser source is divided into pump and Stokes arms, as shown in Figure 3-1. A Faraday isolator (Electro-Optics Technology, Inc., Traverse City, MI) is positioned in the beam path after the Tsunami laser to avoid back reflection; the isolator also adds a positive chirp to the pulse. To compensate for the chirp, angular dispersion (which produces a negative group delay dispersion (GDD)) is introduced, either through a prism compressor or grating compressor. In our case, a custom-built prism compressor consisting of

two prisms is added to the Stokes arm. The group velocity dispersion is calculated using the following equation [32] :

$$T_1(z) = T_0\left[1 + \left(4ln2/L_D\right)^2\right]^{1/2} \quad (3.1)$$

Where T_1 (z) is the laser pulse width after travelling through the dispersive media, T_0 is the input pulse width and $L_D = \frac{T_0^2}{|\beta_2|}$ is the dispersion length. T_1 (z) and T_0 were substituted in Equation (3.1) to obtain the group velocity dispersion β_2, which was calculated as 5731 fs^2/m with a temporal pulse expansion of 253 fs, measured using the auto-correlator. β_2 was substituted in Equation (3.2) [33] to obtain l, and the distance between two prisms apexes to get the negative GDD is:

$$GDD_{\text{prism}} = \frac{\lambda^3}{2\pi c^2}\left[-4l\left\{2\left(\frac{dn}{d\lambda}\right)^2\right\} + 4\left(\frac{d^2n}{d\lambda^2}\right)\left(2d_{1/e^2}\right)\right], \text{ where} \quad (3.2)$$

GDD_{prism} is the group delay dispersion of the prism, λ is the laser wavelength, (dn/dλ) and $\left(\frac{d^2n}{d\lambda^2}\right)$ are the first and second order derivatives of the wavelength dependant refractive index respectively (written in the form of Sellmeier's equation type) and d_{1/e^2} is the beam diameter at $1/e^2$

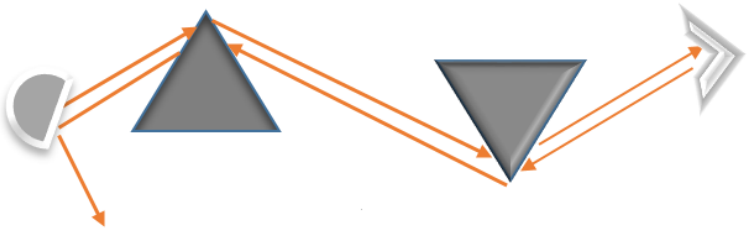

Figure 3-2 Prism compressor setup based on two prisms

In the first prism compressor setup I used two retroreflector mirrors and two prisms. However, the second retroreflector mirror caused spatial beam distortion and I was unable to compress the pulse to less than 126 fs. I addressed this problem by employing only one retroflector mirror to avoid the spatial distortion, and two prisms were applied by varying the distance between them , as shown in Figure 3-2. The distance was set at 39.5 cm, which was the calculated l. I compressed the pulse width down to 87.4 fs with minimal spatial distortion, as shown in Figure 3-3.

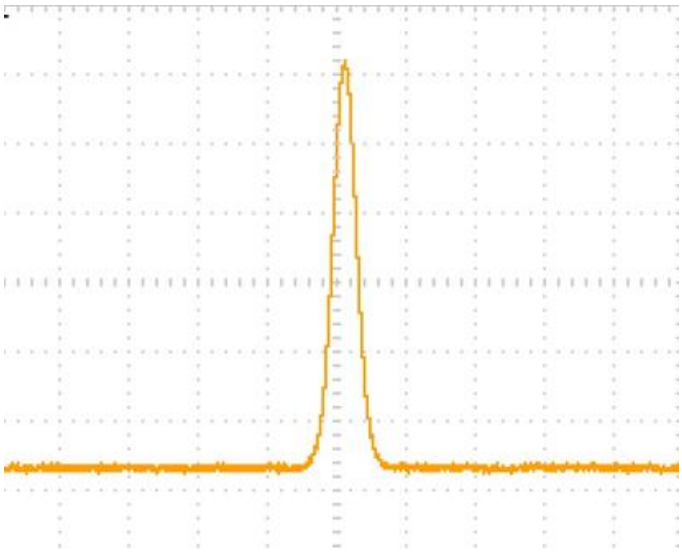

Figure 3-3 Compressed pulse after the prism compressor

The compressed pulse width of 87.4 fs at 800 nm wavelength was coupled into two closely lying zero ZDW supercontinuum PCFs at 775 nm and 945 nm, with 12.5 cm positioned inside a hermetically sealed package (Femtowhite, Crystal Fibre A/S) to generate the Stokes pulse. Figure 3-4 shows the SC rod and the SC spectra with the two zero dispersion wavelengths at 775 nm and 945 nm. The coupling was performed using an X40, 0.65 NA, and 4.5 mm focal length Newport objective lens, and I achieved a coupling efficiency of approximately 40%. For the supercontinuum spectra measurements, an optical spectrum analyzer (OSA) was used to analyze the light from the PCF, collected it with butt-coupled multimode fiber at the output end of the PCF. The measured spectral output of the PCF of the old setup at different average input pump power is shown in Figure 3-5a. The measured spectral output of the PCF with input power was 260 mW at 800 nm, and this was used it to excite the supercontinuum for the CARS microscopy as shown in Figure 3-5b. The spectral power density (SPD) is primarily located in two peaks centered in the visible and IR regions, while there is almost total depletion inside the anomalous dispersion region. I found that the ratio of the intensities of the two peaks depends on how efficiently the light output is collected from the PCF into the multimode fiber in the OSA. Increasing the input power to the PCF causes the outer edges of the supercontinuum to shift outward, as seen in the observations reported earlier [34] [11], and increasing the spectral intensity to 1040 nm also contributes. The beam is collimated at the end of the SC-PCF, and a bandpass filter (Chroma Technologies) is inserted to produce the Stokes pulse at 1040 nm with a bandwidth of approximately 53nm. This specific frequency was selected so the difference between the pump and Stokes frequencies matches the Raman vibrational frequency of 2850 cm^{-1} for the C-H bonds associated with lipid-rich and protein structures. The pump and Stokes

beams overlap spatially and temporally at the dichroic mirror (Thorlabs) and the laser scanning microscope system. Coarse and fine delay lines were inserted into the pump arm to control the temporal overlap of the pump and stokes beams.

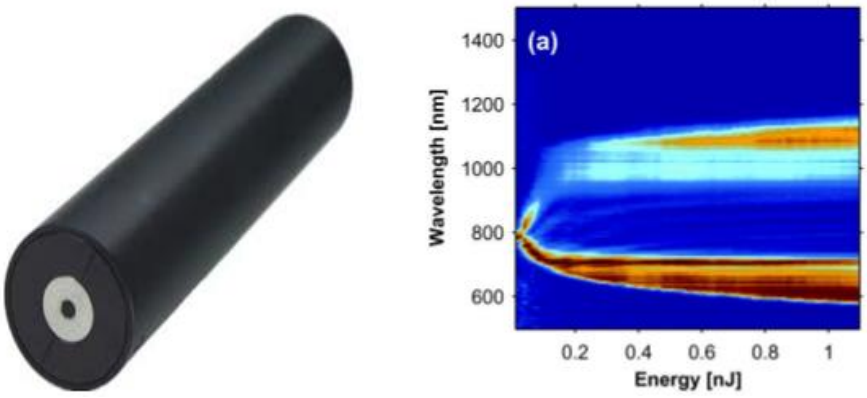

(a) *(b)*

Figure 3-4 shows a) The supercontinuum generation PCF in a sealed rod, b) The supercontinuum generation spectra with two laying zeros at 775 and 945 [34]

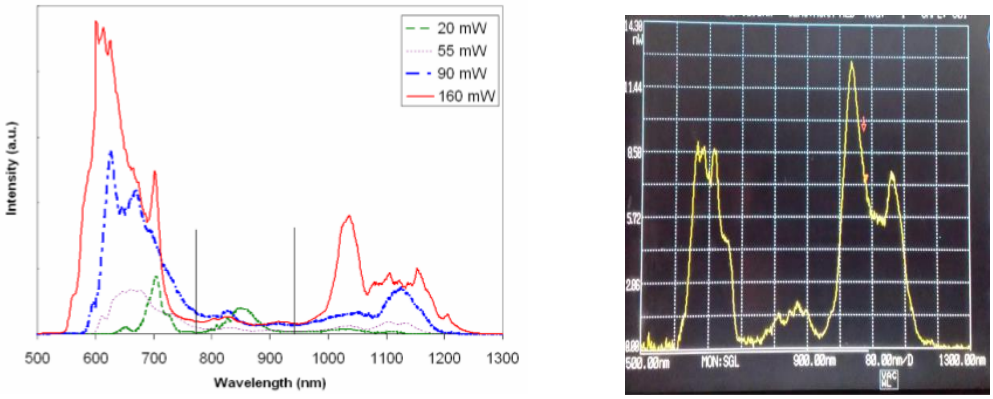

(a) **(b)**

Figure 3-5 Shows two closely lying zero ZDW supercontinuum PCFs, at 775nm and 945nm, a) SCG spectra obtained in early work as a function of the average pump power coupled into the core of the PCF [11], b) measured spectral output of the PCF with optimal power at 260 mW

3.2.2 Laser scanning microscope

The laser scanning microscope is shown in Figure 3-6:

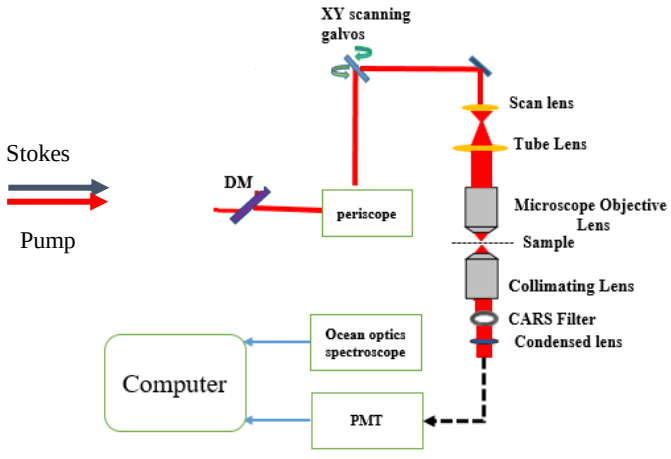

Figure 3-6 Laser scanning microscope

The combined pump and stokes beams are reflected by a dichroic mirror, after which they encounter the two scanning mirrors through the relay, scan and tube lenses. The mirrors are an XY pair of galvanometer mounted mirrors (VM500 GSI Lumonics) that can perform raster scanning, as shown in Figure 3-7. Figure 3-8 shows XY galvanometer 2D sample scanning. The galvanometer mirrors (two vertical mirrors to change the laser level) are positioned after the periscope, and a digital scan controller board SC2000 (GSI Lumonics) is used to control galvo movement by uploading a program to control the speed of raster scanning. While the laser scans across the sample, the detector (R3896 photon multiplier Hamamatsu PMT) collects the emitted photons and sends them to an amplifier (Ortec 9372) and a timing discriminator. This generates short TTL pulses which are transferred to a counter to determine the number of pulses coming from the PMT for image reconstruction. The counting process is done with a Data Acquisition (DAQ) card National Instrument PCI- 6602 DAQ card. The DAQ card transfers the data to the host computer, to allow the laser scanning LabVIEW-based program to begin image reconstruction. Figure 3-9 shows a schematic layout for beam scanning and photon counting.

Figure 3-7 shows XY Galvanometers [35].

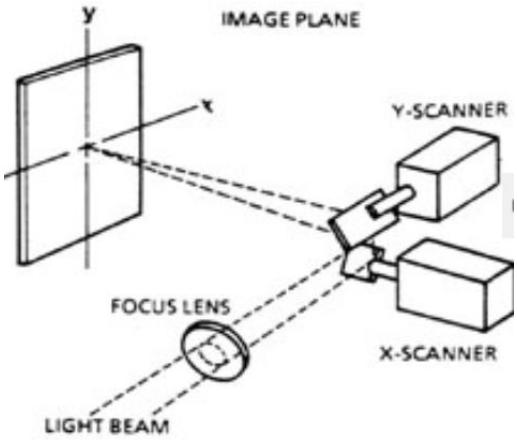

Figure 3-8 A galvanometer scanner scanning a 2D sample [35]

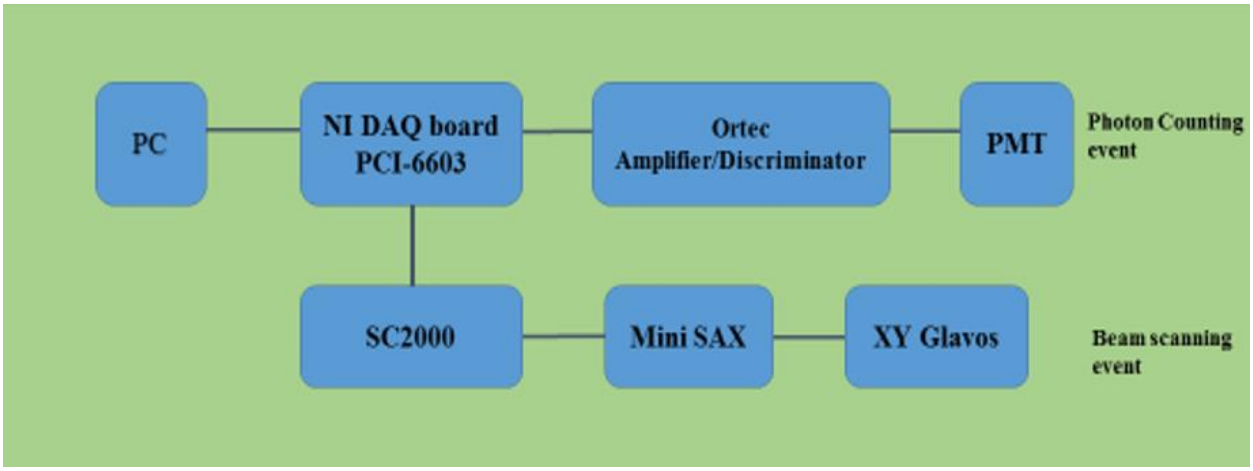

Figure 3-9 Schematic layout for beam scanning and photon counting

3.2.3 Optics Design

The optics design discussed in this section includes the laser system and the microscope design. The overlapped Stokes and pump beams pass through a periscope to the galvanometer level. The periscope is used to lower the laser level at the galvanometer level, and include two adjustable mirrors for the beam alignment. After the overlapped beams pass through the computer-controlled galvanometer, they reach the scan and tube lens for magnification purposes. The collimated beam enters the microscope objective lens and fills its back aperture. With this setup, a water immersion microscope objective lens is used to focus the beam onto the sample, which is placed on a computer controlled 3D translation stage. The forward collection geometry, a20x air objective (Mitutoyo, Japan), collimates the beam before it is spectrally separated by the filter system. An achromatic lens focuses the nonlinear signal onto a multimode collection fiber, which is connected to the Hamamatsu PMT.

3.3 Nonlinear spectroscopy and microscopy results

3.3.1 Introduction

This section presents all the CARS spectroscopy and microscopy results. Section 3.3.2, focuses on CARS spectroscopy optimization using oil immersion sample, while Section 3.3.3 focuses on CARS and TPEF imaging for different samples, and section 3.3.4 focuses on multimodal imaging microscopy for different biological samples.

3.3.2 CARS spectroscopy

In order to detect a CARS signal, it is critical that the microscope is precisely aligned. First, a TPEF signal is obtained using a TPEF dye at 550 nm, which is then put on a #1 microscope coverslip to detect TPEF emission. When emission occurs, I align the collection side of the

microscope until the TPEF signal reaches its maximum peak. Figure 3-10 shows the TPEF signal for the fluorescent dye.

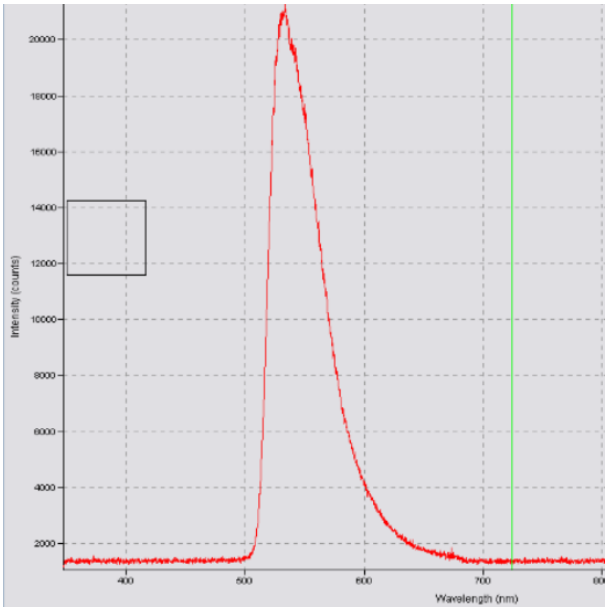

Figure 3-10 Shows TPEF signal for the fluorescent dye

After calibrating the microscope using the TPEF technique, the next step is to detect the CARS signal, which is collected in the forward direction by an air objective lens (Mitutoyo, X20) with immersion oil. The microscope air lens was used because it has a low numerical aperture, which makes the spatial overlap for the pump and Stokes beams inside the objective lens less stringent. The immersion oil (Olympus, Japan) is considered an excellent sample for CARS imaging, as it exhibits low auto-fluorescence and has a high concentration of C-H bonds; thus it can generate a strong CARS signal. After a drop of a immersion oil was put on a #1 microscope cover glass, a CARS signal of 650 nm was detected. It is the filtered and coupled to an Ocean Optics spectrum detector via multimode fiber, as shown in Figure 3-11. The average power of the sample was 67 mW for the pump beam, and ~4 mW for the Stokes beam.

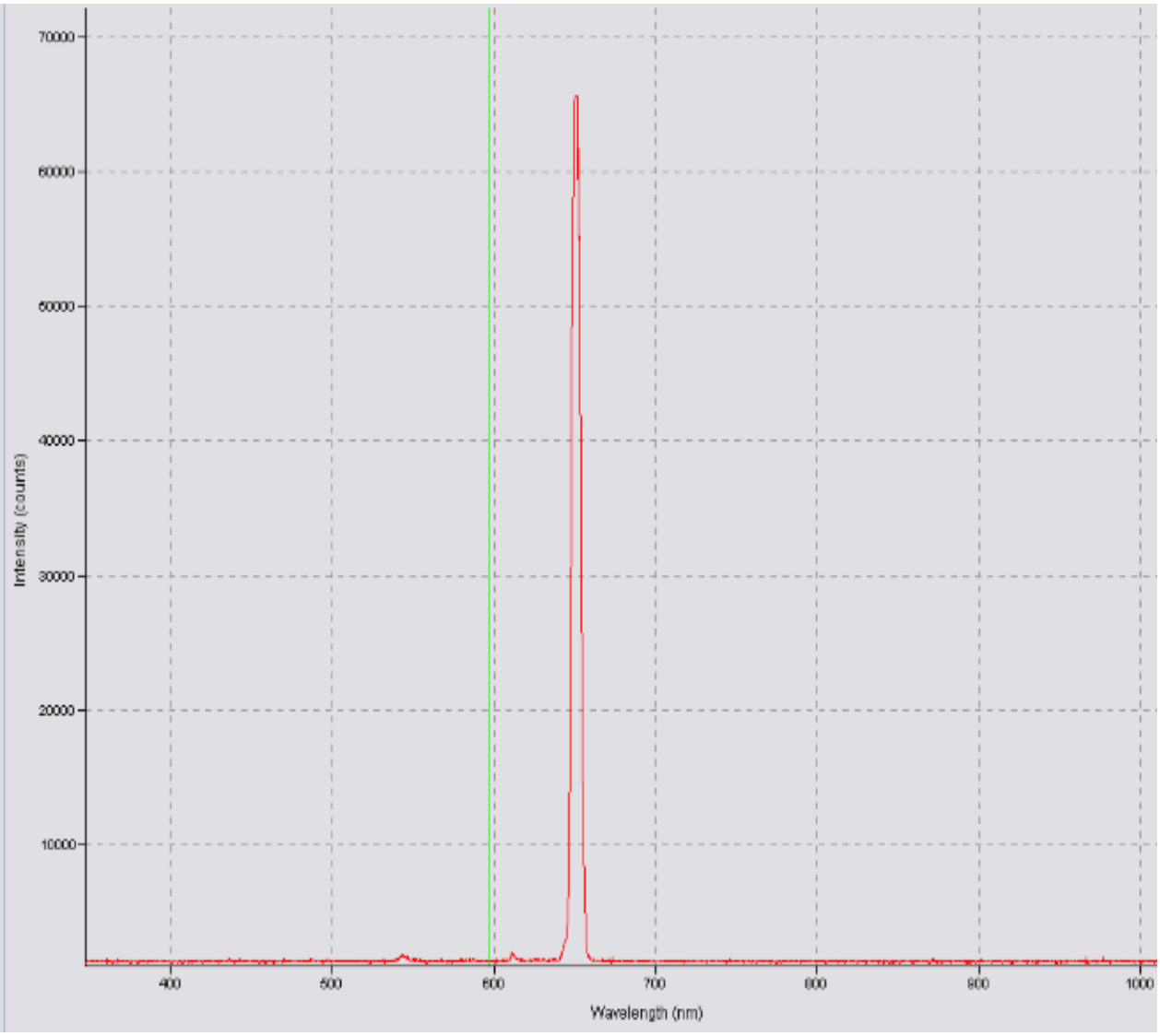

Figure 3-11 The CARS signal for microscope objective oil at 650nm

A spatial overlap of the pump and Stokes beams at the sample focal volume was difficult to obtain. There are many unknown parameters, such as the temporal delay and the correct Z position of the sample. All these parameters must be changed individually, without feedback,

until a CARS signal is detected, after which parameters are optimized beside the microscope collection part to achieve the maximum CARS signal intensity.

3.3.3 Microscope characterization

To test the imaging quality and calibrate the pixel size, I first imaged a United States Air Force (USAF) test slide (Edmund Optics, USA). The sample consisted of sets of three opaque lines, diminishing in size in a fractal-like pattern toward the center, as shown in Figure 3-12 Edmund Optics, "1951 USAF Glass Slide Resolution Targets," 2013 [36]. The Ti-sapphire laser wavelength was set to 800 nm, and the laser power was reduced to 2.3 mW at the USAF target to avoid damaging it. The target was placed upside down toward the objective lens, and the smallest group (group seven) was the area of interest. Once the group seven area was in the field of view, an optimal focus was achieved by moving the sample vertically in 10 µm increments. The transmission image of the USAF target, and the intensity cross-section of the line collection of group seven, are shown in Figure 3-13.

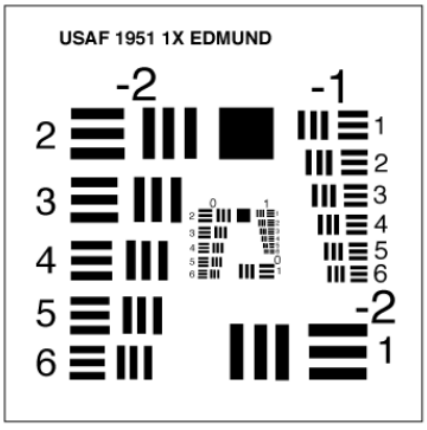

Figure 3-12 1951 USAF resolution target diagram [36]

(a)

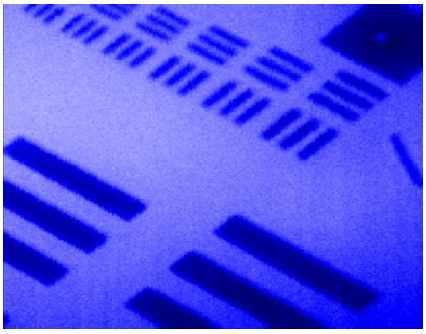

(b)

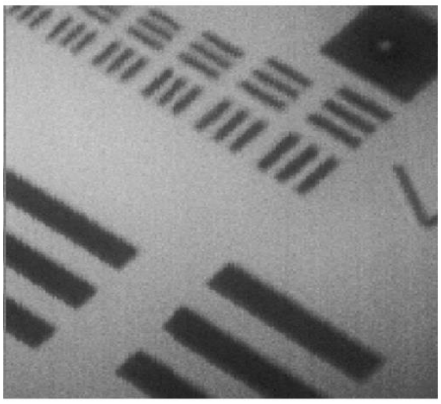

(c)

Figure 3-13 Shows USAF target patterns a) group 4 and 5, b,c) group 7 of USAF pattern

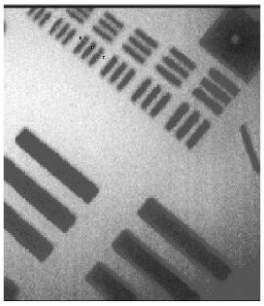

(a)

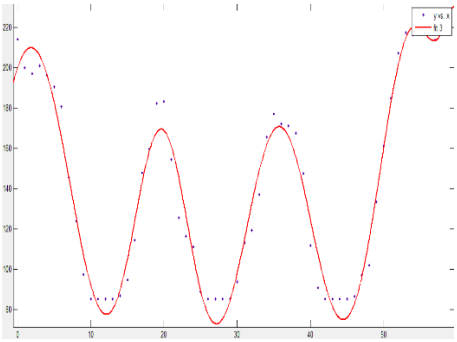

(b)

Figure 3-14 800 nm transmission image of the smallest resolution bars of a 1951 USAF target (b) Intensity cross section of group 7 element 4 markers

Element 4 in group seven had a line spacing of 181 line pairs/mm, which corresponded to a line thickness of 2.76 µm. This technique is used to perform the pixel calibration shown in Figure 3-14(a). From the intensity profile shown in Figure 3-14(b), the distance between two peaks (according to the center of two dark lines shown in Figure 3-14 (a)) is 18 pixels. When compared with the known dark line width of 2.76 µm, the calibration factor was 0.306 µm per pixel

After pixel calibration using laser transmission and testing the image quality, nonlinear imaging of 6 µm fluorescent beads was next.

I first tested our TPEF image quality with green microspheres 6 µm (Polysciences, Inc., USA) fluorescent beads, with the excitation pump wavelength set to 800nm and 18mW average power. These microspheres were chosen because their excitation and emission spectra are suitable for TPEF with the 800 nm Ti-sapphire source, as shown in Figure 3-15. A drop of fluorescent beads was placed on the #1microscope cover glass. Figure 3-16 depicts the results of fluorescent beads

shaped like spheres without significant distortion. This confirmed that the optics and microscope alignment was adequate to produce enough power density to generate TPEF signal from 6 µm fluorescent beads.

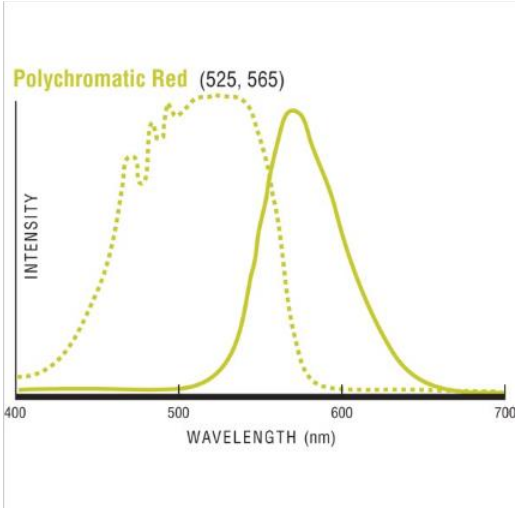

Figure 3-15 Single-photon excitation emission curve for the Fluoresbrite 6um microspheres [26]

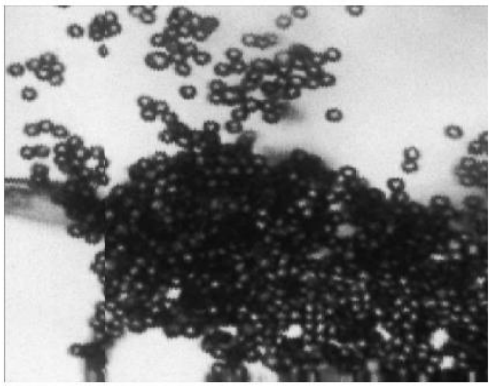

Figure 3-16 TPEF for 6 um fluorescent beads with 265 X 265-pixel image

The first CARS image was for a 20 µm polystyrene-poly bead microsphere (Polysciences, Inc., USA). This type of bead is rich in C-H bonds, and they are good candidates for CARS signal generation. The microspheres were spin coated onto a No. 1 microscope cover glass, and illuminated with 19 mW of pump light and 1.3 mW of Stokes light. Though the captured image of the microspheres, shown in Figure 3-17, shows minimal distortion, there is a shadow close to the poly beads which is likely due to the long exposure time; that is, the sample began to burn.

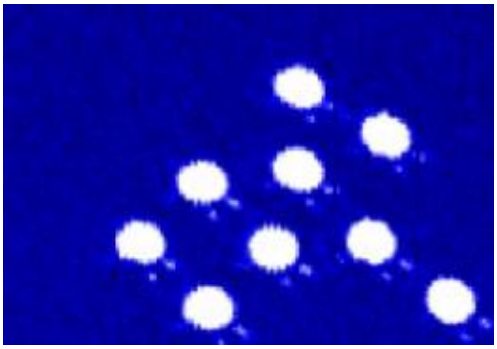

Figure 3-17 CARS image of 20 µm polystyrene microspheres

3.3.4 Imaging of biological samples using multilodal nonlinear microscopy

3.3.4.1 CARS microscopy to image biological sample

After characterizing the microscope and obtaining an acceptable CARS microscopy of 20 um poly beads, I proceeded to image the biological specimen. Figure 3-18 is proof of principle of the developed CARS microscopy setup for imaging biological samples

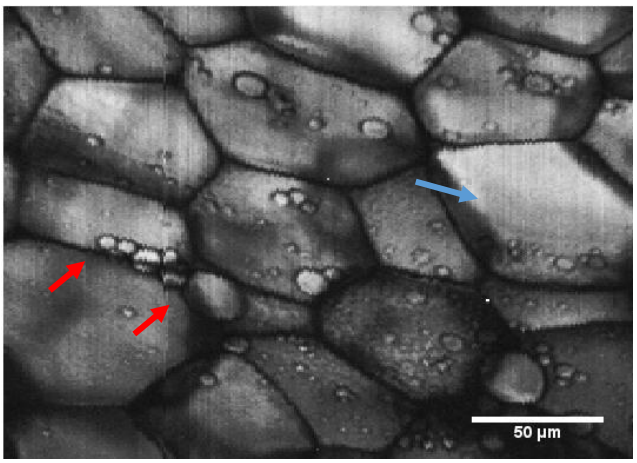

Figure 3-18 CARS image of mouse cell adipocyte. The blue arrow indicates the fat cell, and the red arrow indicates lipid droplets

Figure 3-18 depicts the image of a mouse adipocyte cells, with a single frame collection time of a 256x256 pixel image of ~7 seconds. A 645 nm bandpass filter was added to capture CARS photons only. As shown in the figure, the fat cells and the lipid droplets are clearly indicated by the blue and red arrows respectively. To ensure that the captured image was CARS image, the Stokes beam was blocked and the signal disappeared. This confirmed that the captured photons are CARS, and that the photons generated by TPEF were completely blocked by the 645 nm bandpass filter.

3.3.4.2 SHG microscopy

Collagen in a cow tail tendon sample was used for the SHG microscopy. A thin slice of the tendon was cut and placed between two #1 microscope cover glasses. An 800 nm beam with 35 mW power was directed at the sample through the pump arm, and an air microscope objective lens (Mitutoyo, 20x, 0.42NA) was used for the imaging. Sample emissions were collected and the signal was separated from the excitation beam by positioning a low-pass filter at 680 nm (Chroma, Technology) after the Mitutoyo collimating lens. A short pass filter at 485 nm was

placed after the 680 nm filter to collect the second harmonic generation signal from the collagen of the tendon sample.

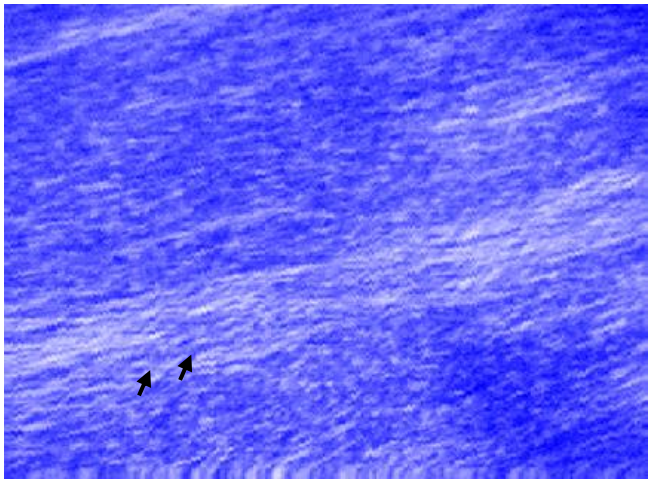

Figure 3-19 SHG image of collagen in cow tendon tail, arrows indicate individual strands

The peak for the SHG signal is 400 nm, since the pump wavelength is 800 nm and the frequency doubling for 800 nm wavelength is 400 nm. As it is non-centrosymmetric with excessive nonlinear susceptibility, collagen has a natural second harmonic signal. Imaging the biological sample with SHG microscopy reveals unfixed and unstained tissues at a resolution as fine as that of processed histologic sections. Figure 3-19 shows an SHG image of collagen in a tail tendon, with arrows identifying individual strands.

3.4 Challenges during image acquisition

It was difficult to obtain high-resolution images. It took a long time to make the LabVIEW program for image acquisition compatible with the hardware (6602 NI- DAQ wiring, and XY

Galvos). As shown in Figure 3-20, when the image reconstruction program began to respond to the laser scanning system, the first image I obtained for 6um fluorescent beads was elliptical and striped, and the image dimensions were not 256 x 256 pixels full frame

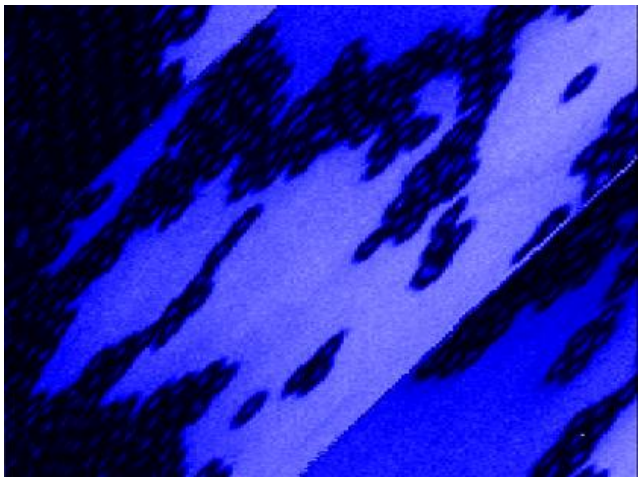

Figure 3-20 Shows the first image acquired for 6um beads, with distortion

These results indicated that there was a lack of synchronization between the X and Y scanning. At the beginning of each scan, the frame sync line is triggered at the start of every frame to make the y-galvo jump back to the top of the frame, while the x sync line is triggered at the start of every line to make the x-galvo sweep out a line. This continues until a full frame (256 x 256 pixels) is achieved. The stripes are due to either a lack of synchronization between the X and Y scanning or between the scanning program and the signal from the PMT, or incorrect wiring in the NI- DAQ -6602 accessories NI-SC2000 board. I rechecked every hypothesis until I found the source of the problem: the laser scanning microscope LabVIEW based program was acquiring data faster than the data coming in from the Hamamatsu PMT. To test this, I added different delays in the LabVIEW program, and the effect was remarkable. Figures 3-21(a) and (b) show 6um bead images with delays of 100 and 200 µs, respectively.

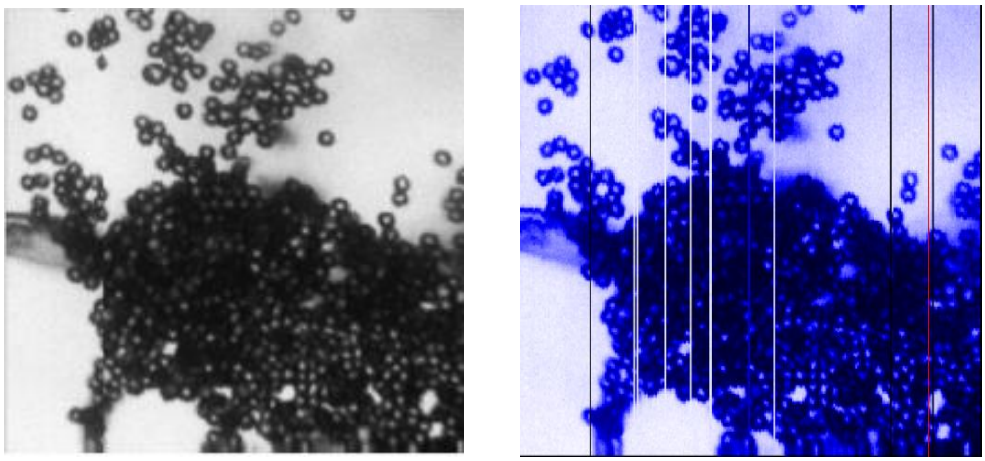

(a) (b)

Figure 3-21 Images of 6um beads with a) 100 microsecond delay, b) 200 microsecond delay added

After performing numerous calculations and measurements to determine the optimal delay, I found that adding a 100 μs delay to the Y line in the LabVIEW program gave me correct imaging. To start image re-construction, a counter sends pulses to the LabVIEW program to read the TTL pulses from PMT every 92 µs. The Y line takes 92 µs on the scanning screen to scan one line in the Y direction. Thus, scanning an entire frame of 256 pixels takes approximately 25.5 s, which is the same time required to finish scanning one frame. However, without adding any delay the time to finish one frame was 6.4s, which means it took 25 µs to scan one y line; this is not enough to scan all the pixels and collect all the incoming data coming from the PMT. As a result, I added 100 ms to the Y line in the LabVIEW program, thereby ensuring that there is time to read all the photons coming from the PMT, and subsequently obtain acceptable image reconstruction.

3.5 Conclusion

The experiment setup and results were performed using the multimodal, nonlinear imaging setup described. After pixel calibration, different samples were imaged using CARS, TPEF and SHG microscopy techniques. The challenges of scanning microscopy were addressed with this solution.

Chapter 4 : Integration of a portable miniaturized nonlinear endoscope with a femtosecond fiber laser

4.1 Introduction

In this chapter, I present the integration of a portable miniaturized nonlinear imaging microscope for endoscopy applications with an all-normal dispersion femtosecond fiber laser. In Section 4.2, the rationale behind the integration is discussed, Section 4.3 describes the femtosecond fiber laser characteristics. Section 4.4 explains the experimental setup of the endoscope driven by femtosecond fiber laser, while Section 4.5 presents the imaging results of this compact imaging system. Finally, Section 4.6 explains the conclusions.

4.2 Rationale behind the Integration

Brett Smith, a graduate student from our lab, demonstrated a novel, miniaturized and multimodal CARS microscope (endoscope) based on MEMS scanning mirrors and custom miniature optics. High-resolution images of CARS, TPEF and SHG in the epi direction from different samples were obtained successfully [14]. The ultrafast laser used to drive the endoscope is a Ti-Sapphire, and though it is an excellent tool, its application has been restricted to the laboratory environment because it is bulky, expensive and requires very precise optical alignment. Thus, this laser is actually a significant impediment to building a portable biological imaging system.

In parallel of building the miniaturized nonlinear endoscope, another group from our lab, Hussein Kotb and Mohamed Abdelalim, were focused on constructing a compact, ultrafast laser to replace the Ti-Sapphire laser source. Femtosecond fiber lasers are a promising alternative to solid-state lasers, as they are compact, do not have alignment issues and are less expensive. Though many researchers have worked with femtosecond fiber lasers in multi-photon microscopy [37] [38], Kotb and Abdelalim were motivated by the need for a femtosecond fiber laser that can be used for the nonlinear imaging applications [39].

Driving multi-photon endoscopes by femtosecond all-fiber lasers is a critical step toward building low cost bedside imaging systems. Moreover, integration of the endoscope and all-fiber lasers can potentially be applied to many other practical purposes.

4.3 Femtosecond fiber laser characteristics

I used a homebuilt single Yb^{+3} doped femtosecond all-fiber laser as the light source to produce TPEF. The fiber laser operates at 1030 nm, and delivers 100 mW average power and a 170 femtosecond pulse width with a 23 MHz repetition rate. Figure 4-1 (a, b, c) shows the 59.5x 34.5x5.4 cm^2 femtosecond fiber laser device, the autocorrelation trace of the 170fs pulse and the pulse spectrum, respectively. Building a 1030 nm wavelength femtosecond fiber laser has many advantages. As mentioned previously, longer wavelength excitation for multiphoton microscopy decreases tissue scattering, and increases the imaging depth in a thick tissue. It can also be used to excite additional fluorescent proteins and dyes developed for traditional microscopes. Since the main constituent of biological tissue is water, an optical window of ~1μm was selected as the center of the laser because the light produces minimal water absorption.

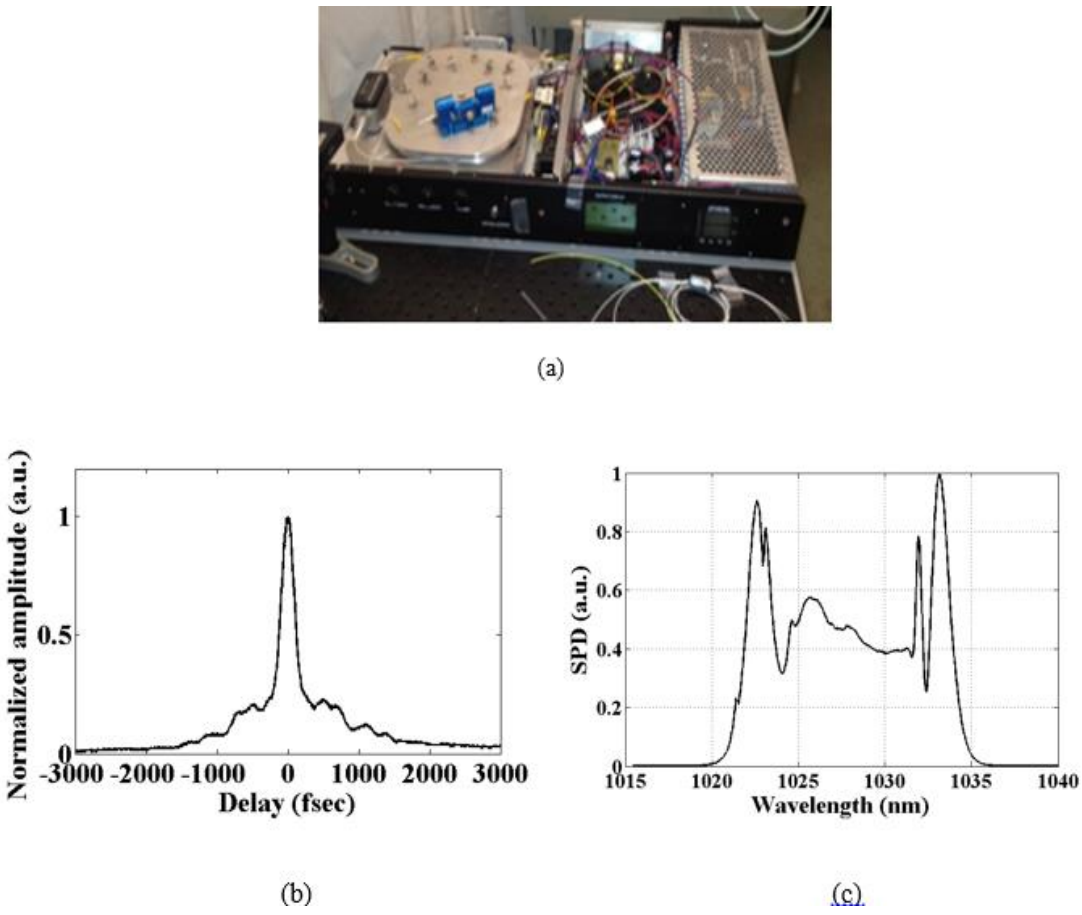

Figure 4-1 The homebuilt the 59.5x 34.5x5.4 cm2 femtosecond fiber laser device built by Ph.D. student Hussien Kotb, b) the autocorrelation trace of 170fs pulse, and c) the 170fs pulse spectrum

The fiber laser constructed in our lab is an all-normal dispersion mode-locked fiber laser that generates chirp pulses. The length of the Yb^{+3} fiber (L_{Yb}) is 37.5 cm, the SMF (L_{SMF2}) is 39.5 cm long, and β_2 and β_3 are 24690.1 fs^2/m and 75.3 fs^3/m for the SMF, and 32550.1 fs^2/m and 79.6 fs^3/m for Yb^{+3} fiber, respectively.

4.4 Experimental Setup Description

As shown in Fig. 4-2, two set-ups are demonstrated for comparison purposes. The Ti: sapphire laser source delivers excitation light to the endoscope through various optics components, as depicted in Figure 4-2(a) [14], while the compact all-normal-dispersion femtosecond all-fiber

laser used for the same purpose is shown in Figure 4-2(b). The Ti sapphire laser in Figure 4-2(a) produces a transform limited ~70 fs pulse train at 80 MHz repetition. As described in detail by Smith et al. [40], 22 mW of light at ~800 nm is used as the excitation light in the pump arm to generate the TPEF signal. The miniature objective lens in the endoscope was designed to enable in-vivo imaging of rat spinal cord, and the distal end cannot have an outer diameter greater than 3.0 mm.

The early work of Smith et al. [14] provides a detailed description of the endoscope setup driven by the Ti: Sapphire laser source. The femtosecond fiber laser, designed and built in our lab, replaces the Ti: sapphire laser. I used a hollow core photonic crystal fiber to compress the output pulse, and coupled it with the endoscope through an FC/APC connector, as shown in Fig. 4.2(b). The signal was collected in the epi direction from the sample, which was mounted on a three-axis computer controlled stage, and directed to a multimode fiber mounted on the endoscope body. The signal was delivered through the multimode fiber to a photomultiplier tube (PMT) (Hamamatsu R3896) with a 680 nm short pass filter (ET680SP-2P8, OD5, Chroma Technology) mounted inside to eliminate excitation light.

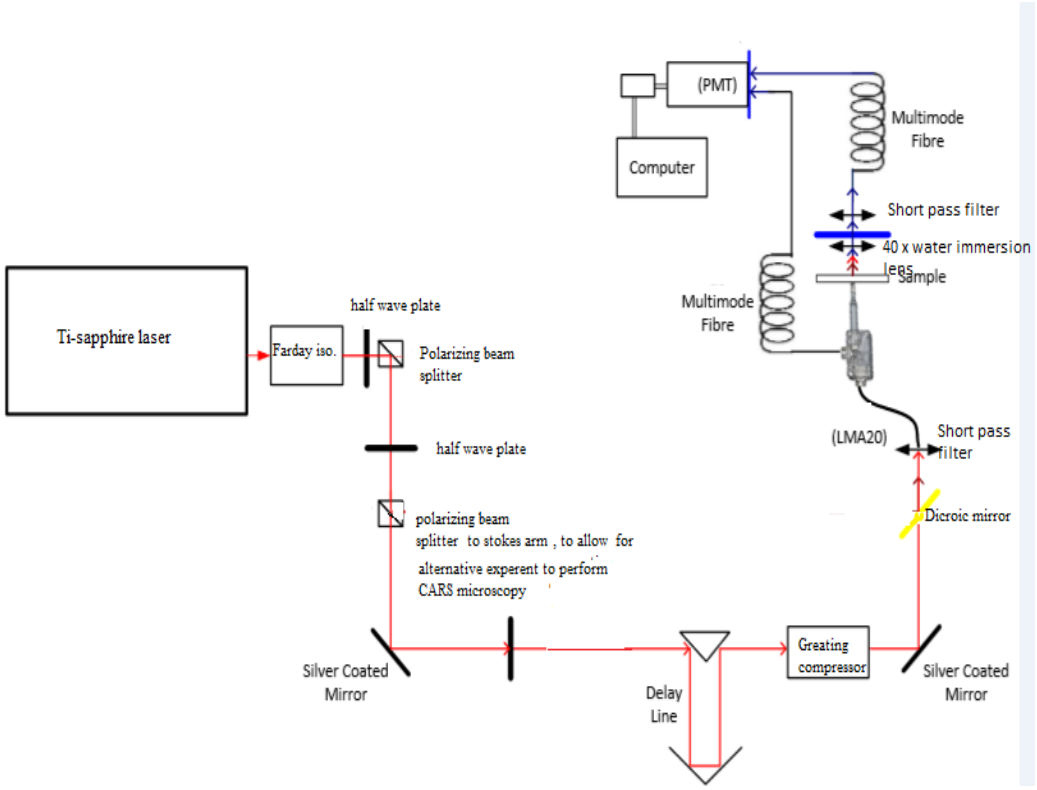
(PMT)
Computer
Multimode Fibre
Short pass filter
40 x water immersion lens
Sample
Multimode Fibre
Ti-sapphire laser
Farday iso.
half wave plate
Polarizing beam splitter
half wave plate
polarizing beam splitter to stokes arm , to allow for alternative experent to perform CARS microscopy
(LMA20)
Short pass filter
Dicroic mirror
Silver Coated Mirror
Delay Line
Greating compressor
Silver Coated Mirror

(a)

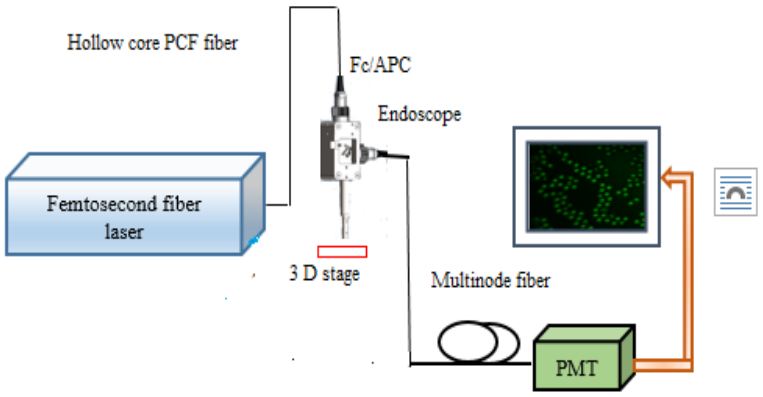

(b)

Figure 4-2 Two endoscope experimental setups used for TPEF: (a) Ti-sapphire laser drives the endoscope through the following components: 1) Ti: Sapphire laser source, (2) FI Isolator, (3) Half wave plate, (4) Polarizing beam splitters, (5) Prism compressor, (6) 440X microscope objective lens, (7) SC- PCF, (8) Aspheric 5 mm focal length lens, (9) 1040 nm central wavelength band-pass filter, (10) Grating Compressor, (11) Short pass dichroic mirror, (12) 5X microscope objective lens, (13) LMA 20 PCF, (14) Endoscope, (15) 40X water immersion lens, (16) Multimode collection fibre, (17) Short-pass Filter, (18) Hamamatsu PMT, (19) Discriminator and field programmable gate array. (b) Femtosecond fiber laser setup that drives the endoscope.

4.5 Results and Discussion

I tested the integration of the femtosecond fiber laser with the endoscope by taking TPEF images of 6μm diameter fluorescent beads. TPEF imaging was chosen because the femtosecond fiber laser can generate a single wavelength of 980 nm, and I wanted to test with the TPEF imaging technique before tailoring it to CARS. The beads were diluted with water, then mounted on a thin glass coverslip. The average power from the laser to the input of the endoscope was approximately 100 mW, with a pulse width of 170 fs near the 980 nm wavelength. The beads were exposed to an average power of ~22 mW of 980 nm light, and

focused to a 1 μm spot on the bead sample with the miniaturized water-immersion objective of the endoscope.

I imaged a TPEF for the 6 μm beads using the femtosecond all-fiber laser as a light source, with 512×512 pixel resolution, as shown in Figure 4-3(a). The intensity profile for a single bead was plotted using image J, an image processing tool. A curve fitting with the Gaussian profile was applied to a single bead intensity profile, and Matlab was used to determine the bead's FWHM, which was found to be 6.9 μm, as shown in Fig. 4-7(b). For comparison, the same bead sample was then imaged with the Ti: sapphire laser at 800 nm light and 100 fs pulse width, with an average power of ~12mW in the epi direction, using the experimental setup shown in Fig. 4-2 (a). The plot of the resulting image is shown in Fig. 4-3 (c). There is reasonable agreement in the results of the TPEF image of the beads obtained using the two set-ups. The TPEF images are magnified by a factor of ~1.15, and the image taken with the femtosecond fiber laser has more aberrations. The aberration difference could be due to the variance in the mode field diameter (MFD) of the photonic bandgap (PBG) fiber (HI-1060) that delivers the light, and the expected MFD of the input at the endoscope. The input of the endoscope is designed to be connected to an LMA20 fiber with a 0.06 numerical aperture (NA), while the PBG fiber (HI-1060) used to deliver the output of the femtosecond fiber laser has an NA of 0.2. In addition, the TPEF generating the signal for the 6μm fluorescent beads is more efficient at 800nm laser wavelength than the 980nm laser. The difference in divergence angles in the endoscope and the beads generating the signal efficiency at 980nm wavelength, has an impact on image quality and the size of the measured bead.

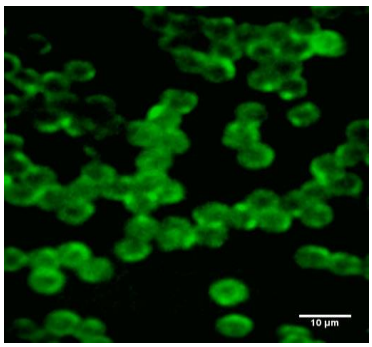

(a)

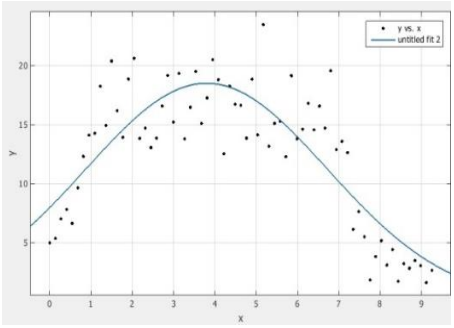

(b)

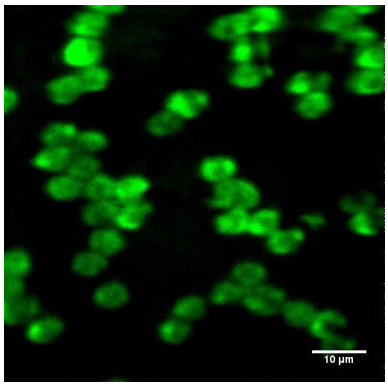

(c)

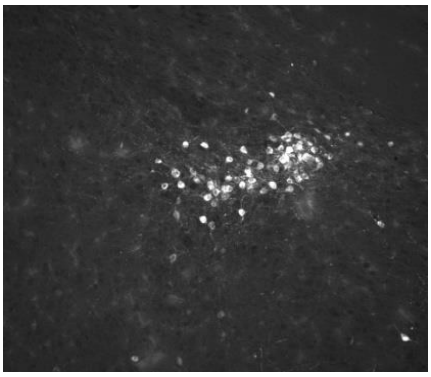

(d)

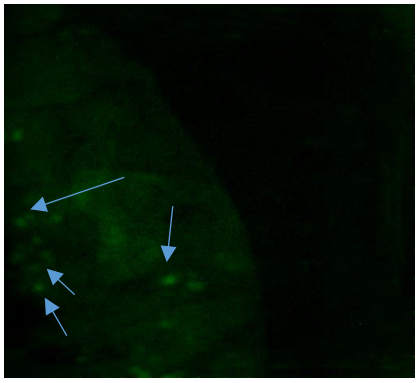

(e)

Figure 4-3: a) TPEF microscopic imaging of 6 µm fluorescent beads using the femtosecond fiber laser, b) intensity distribution in the 6 µm fluorescent beads with an FWHM of 6.9µm obtained by femtosecond fiber laser, c) TPEF image of 6 µm bead sample using Ti-sapphire laser as shown in Fig.2(a), d) In vitro imaging of 5 µm thin section of mouse neuronal tissue labelled with Alexa488 and imaged with confocal fluorescence microscope, e)In vitro TFEF image of the same sample as in Fig.4d, using femtosecond fiber laser, with the arrows pointing at the neurons.The field of view is 70x70 µm.

I then tested the integrated femtosecond fiber laser endoscope setup to demonstrate TPEF imaging of a biological sample. Figure 4-3(d) shows a confocal fluorescence image of a 5 μm thin section of mouse neuronal tissue labeled with Alexa488, obtained using a commercial microscope. The TPEF image in Figure 4-3(e) shows bright features (indicated by arrows) that correspond to the labeled neurons in the sample. The proof of concept TPEF image demonstrates the potential of our integrated system to perform nonlinear imaging of biological samples.

4.6 Conclusion

In this chapter, I explored replacing the Tsunami laser that drives the nonlinear microscope/endoscope with a compact fiber laser source of 980 nm. I analysed the TPEF images of 6μm diameter fluorescent beads and a sample of labeled neurons in a 70 x 70 μm field of view. Comparisons of the images obtained by the all-fiber laser-driven endoscope system, and those achieved by the endoscope driven by Ti-sapphire laser, show reasonable agreement. Using different laser delivery fibers that match the mode field diameter of the endoscope and the femtosecond fiber laser, will significantly increase image resolution and quality. Future work on our integration setup could achieve 3D nonlinear imaging of biological samples, and modify the system to perform CARS imaging. The small footprint, low cost and ease of use will bring multimodal nonlinear imaging closer to clinical application.

Chapter 5: Summary and future work

5.1 Summary

The first objective of this thesis is to describe the reconstruction of our multimodal nonlinear optical microscope in our new photonics lab, and to depict the images obtained using our multimodal microscope. This microscope includes CARS, TPEF and second harmonic generation modalities. The second objective is to integrate our miniaturized nonlinear microscope with a Femtosecond fiber laser.

Chapter one introduces the nonlinear imaging modalities using nonlinear imaging microscopy. This chapter also shows the benefits of nonlinear optical microscopy over other imaging techniques.

Chapter two provides a background of nonlinear microscopy and the generation of nonlinear optical processes. The basics of each nonlinear process in our multimodal nonlinear microscope SHG, TPEF, CARS, and supercontinuum generation is briefly reviewed.

In chapter three, the major components of CARS microscopy/spectroscopy experimental setup are explained. The multimodal nonlinear imaging microscopy results, and the challenges that I faced are also presented in this chapter.

In Chapter 4, a fiber delivered handhold multimodal miniaturized endoscope was integrated with homebuilt femtosecond fiber laser, and tested. System functionality was demonstrated successfully, and proof-of-concept images were done by obtaining the TPEF imaging for chemical and biological samples in the epi-direction.

In conclusion, CARS microscopy has the potential to become used widely for a variety of biomedical applications

5.2 Future work

In this thesis, the imaging results of the integration of the femtosecond fiber laser and the nonlinear endoscope was limited to TPEF. This is because the femtosecond fiber laser was limited in power. The next step would be to develop a higher power femtosecond fiber laser that can be used to generate both the pump and Stokes to generate CARS spectroscopy/microscopy. That can be done by dividing the output of the excitation source based on femtosecond fiber laser into two arms: one arm for the pump and the second arm for Stokes. A highly nonlinear PCF fiber can be introduced, to generate longer wavelength band. In this case the arm will served as a Stokes arm. The other arm will be considered as a pump arm. That technique can provide the opportunity to use this femtosecond fiber laser to perform single laser source for CARS microscopy. The ability to perform various modalities (TPEF, CARS, SHG) using a portable femtosecond fiber laser and an endoscope will bring the multimodal nonlinear imaging closer to clinical application.

To improve the current CARS microscopy setup, it is useful to develop CARS spectral focusing at lower vibrational frequencies ($700cm^{-1}$- $1800\ cm^{-1}$) in order to have access to the fingerprint region. Chirping the input pulses for the SC-PCF in the Stokes arm, can generate supercontinuum with closer peaks of the two-ZDWs to the pump wavelength. With this technique, we can use 800 nm pump pulses without the need for transform-limited pulses. Faster XY scanners, and more sensitive PMT can also improve the imaging system.

The next improvements on the multimodal nonlinear endoscopy will focus on reducing the optical aberrations of the system, reducing endoscope size by using more miniaturized optics. With more advancement in miniaturized laser scanners, micro- optics, nonlinear PCF, and femtosecond fiber laser will assist in developing a compact fiber based nonlinear imaging microscopy/endoscopy.

.

References

[1] C. L. Evans and S. X. Xie, "Coherent anti-stokes Raman scattering microscopy: chemical imaging for biology and medicine," *Annu.Rev.Ana.Chem.*, pp. 883-909, 2008.

[2] C. L. Evans, E. O. Potma, M. Puoris'haag , D. Cote, C. P. Lin and S. X. Xie, "Chemical imaging of tissue in vivo with vedio- rate Coherent Anti-Stokes Raman Scattering microscopy," *Annual review of analytical chemistry*, vol. 102, no. 46, pp. 838-909, 2005.

[3] L. G. Rodriguez, S. J. Lockett and G. R. Holtom, "Coherent anti-stokes Raman scattering microscopy," *Cyto.A. biological review*, vol. 69A, no. 8, pp. 779-791, 2006.

[4] J. Cheng and S. X. Xie, "“Coherent Anti-Stokes Raman Scattering Microscopy: Instrumentation, Theory, and Applications," *J. Phys. Chem.*, no. 108, pp. 827-840, 2004.

[5] M. Chemnitz, M. Baumgartl, T. Meyer, C. Jauregui, B. Dietzek, J. Popp, J. Limpert and and Andreas Tünnermann, "Widely tuneable fiber optical parametric amplifier for coherent anti-Stokes Raman scattering microscopy," *Opt. Express*, vol. 20, no. 24, pp. 26583-26595, 2012.

[6] P. Marker and R. Terhune, "Study of optical effects due to an induced polarization third order in the electric field strength," *Phys. Rev.*, vol. 137, pp. A801-A818, 1965.

[7] R. F. Begley, A. B. Harvey and R. L. Byer, "Coherent Anti-Stokes Raman Spectroscopy," *Appl.Phys.Lett.*, vol. 25, pp. 387-390, 1974.

[8] M. D. Duncan, J. Reintjes and and T. J. Manuccia, "Imaging biological compounds using the CARS microscope," *Opt. Engineering,* vol. 24, no. 2, pp. 352-355, 1985.

[9] A. Zumbusch, G. R. Holtom and X. S. Xie, "Three-dimensional vibrational imaging by coherent anti-Stokes Raman scattering," *Phys.Rev.Lett.*, vol. 82, pp. 4142-4145, 1999.

[10] J. X. Cheng, A. Volkmer, L. D. Book and S. X. Xie, "An epi-detected coherent anti-Stokes Raman scattering (E-CARS) microscope with high spectral resolution and high sensitivity," *J.Phys. Chem. B,* vol. 105, no. 7, pp. 1277-1280, 2001.

[11] S. Murugkar, C. Brideau, A. Risdale, M. Naji and H. Anis, "Coherent antiStokes Raman scattering microscopy using photonic crystal fiber with two closely lying zero dispersion wavelengths," *Optics Express,* vol. 15, no. 21, pp. 14028-14937, 2007.

[12] B. A. Flushberg, J. C. Jung, E. D. Cocker, E. P. Anderson and M. J. Schnitzer, "In vivo brain imaging using a portable 3.9 gram two-photon fluorescence microendoscope," *Optics Letter,* vol. 30, no. 17, pp. 2272-2274, 2005.

[13] M. Myaing, D. MacDonald and X. Li, "Fiber-optic scanning two-photon fluorescence endoscope," *Optics Letter,* vol. 31, no. 8, pp. 1076-1078, 2006.

[14] B. Smith, N. Majid, S. Murugkar, C. Brideau, P. K. Stys and H. Anis, "A novel multimodal CARS miniaturized microscope," *Proced. SPIE,* no. 8226, 2012.

[15] W. B. Robert, Nonlinear Optics, 3rd edition Elsevier, 2008.

[16] Nonlinear spectroscopy, "Nonlinear spectroscopy," Genia photonics, [Online]. Available: ,

http://www.geniaphotonics.com/business-markets/life-sciences/nonlinear-spectroscopy/.

[17] Xie, "Coherent Raman imaging,," Harvard University, [Online]. Available: https://bernstein.harvard.edu/research/cars-why.htm.

[18] B. R. Masters, P. T. C. So and E. Gratton, "Multiphoton excitation fluorescence microscopy and spectroscopy of in vivo human skin," *Biophysics,* vol. 72, pp. 2405-2412, 1997.

[19] J. Garcia, F. Zhang and P. C. Ford, "Multi-photon excitation in uncaging the small molecule bioregulator nitric oxide," *Philosophical Transactions of the Royal Society A: Matmatical, Physical and Engineering Sciences,* vol. 371, 1995.

[20] C. Sheppard, J. Gannaway, R. Kompfner and and D. Walsh, "Scanning harmonic optical microscope," *Ieee J Quant Elect,* p. D100, 1977.

[21] S. Roth and and I. Freund, "Coherent optical harmonic-generation in rat-tail tendon," *Opt Commun,* vol. 33, p. 292–296, 1980.

[22] P. J. Campagnola and and L. M. Loew, "Second-harmonic imaging microscopy for visualizing biomolecular arrays in cells, tissues and organisms," *Nat Biotechnol,* vol. 21, no. 11, p. 1356–1360, 2003.

[23] P. Campagnola, "Second Harmonic Generation Imaging Microscopy: Applications to Diseases Diagnostics," *Anal Chem,* vol. 83, p. 3224–3231, 2011 May 1.

[24] W. Kaiser and C. G. Garrett, "Two-photon Excitation in CaF2:Eu2+," *Phys. Rev. Lett.,* pp.

229-232, 1961.

[25] F. Helmchen and and W. Denk, "Deep tissue two-photon microscopy," *Nat. Methods,* vol. 2, no. 12, pp. 932-940, 2005.

[26] T. Boulesteix, A.-M. Pena, N. Pagès, G. Godeau, M.-P. Sauviat, E. Beaurepaire and and M.-C. Schanne-Klein, "Micrometer scale Ex Vivo multiphoton imaging of unstained arterial wall structure," *Cytometry,* vol. 69A, no. 1, pp. 20-26, 2006.

[27] "Fluoresbrite,Polychromatic Red Microspheres 1.0µm," polysciences Inc, [Online]. Available: http://www.polysciences.com/default/fluoresbrite-polychromatic-red-microspheres-6um.

[28] E. O. Potma and S. X. Xie, "Direct visualization of lipid phase segregation in single lipid bilayers with coherent anti-Stokes Raman scattering microscopy.," *Chem. Phys.*, vol. 6, no. 1, pp. 77-79, January 14 2005.

[29] Wikibidia, "Electromagnetic absorption by water," [Online]. Available: https://en.wikipedia.org/wiki/Electromagnetic_absorption_by_water.

[30] R. R. Alfano and S. L. Shapiro, "Emission in the region 4000 to 7000 Å via four-photon coupling in glass," *Phys. Rev. Lett,* vol. 24, pp. 584-587, 1970.

[31] R. R. Alfano and and S. L. Shapiro, "Observation of self-phase modulation and small-scale filaments in crystals and glasses," *Phys. Rev. Lett.,* vol. 24, p. 592–594, 1970b.

[32] G. P. Agrawal, Nonlinear Fiber Optics,, 5th e ed., Rochester, NewYork: Elsevier, 2013.

[33] N. S. Physics, "Prism Compressor for Ultrashort Laser Pulses," Newport Corporation.

[34] K. Hilligsoe, T. Andersen, H. Paulsen, C.Nielsen, K. Molmer, S. Keiding, R. Kristiansen, K. Hansen and and J. Larsen, "Supercontinuum generation in a photonic crystal fiber with two zero dispersion wavelengths," *Opt. Express,* vol. 12, no. 6, p. 1045 – 1054, 2004.

[35] "Image of XY galvanometer," National Instruments, [Online]. Available: http://sine.ni.com/cs/app/doc/p/id/cs-14886#prettyPhoto[gallery]/1/.

[36] "Image of 1951 USAF Target," Edmund Optics,, [Online]. Available: http://www.edmundoptics.com/testing-targets/test-targets/resolution-testtargets/1951-usaf-glass-slide-resolution-targets/1790.

[37] K. Kieu, S. Mehravar, R. Gowda, R. A. Norwood and and N. Peyghambarian, "Label-free multi-photon imaging using a compact femtosecond fiber laser mode-locked by carbon nanotube saturable absorber," *Biomedical optics express,* vol. 4, p. 2187, October 1(2013).

[38] E. K. Hussein, A. A. Mohamed and A. and Hanan, "An Efficient Semi-Vectorial Model for All-Fiber Mode-Locked Femtosecond Lasers Based on Nonlinear Polarization Rotation,," *Journal of selected topics in quantum electronics,,* vol. 20, 2014.

[39] H. E. Kotb, M. A. Abdelalim and H. Anis, "Effect of mode locking technique on the filtering bandwidth limitation in all normal dispersion femtosecond fiber laser," *Photonic west,* 2014..

[40] S. Brett, " master thesis, Coherent Anti-Stokes Raman Scattering Miniaturized

Microscope,," 2013.

[41] "Supercontinuum generation fiber devices," Newport, [Online]. Available: https://www.newport.com/f/supercontinuum-fiber-module-femtowhite.

[42] L. Moreau, O. Sandre, S. Charpak, M. Blanchard-Desce and J. Mertz, "Coherent scattering in multiharmonic light microscopy," *Biophysics Journal,* no. 80, p. 1568–1574, 2001.

[43] X. Nan, W. Y. yang and S. Xie, "CARS microscopy: lights up lipids in living cells," *Biophotonics International,* 2004.

[44] H. Kotb, M. A. Abdelalim and H. Anis, "“Effect of mode locking technique on the filtering bandwidth limitation in all normal dispersion femtosecond fiber laser," *Photonic West,* 2014.

[45] W. Denk, . J. . H. Strickler and . W. . W. Webb, "Two-Photon Laser Scanning Fluorescence Microscopy," *Science,* vol. 248, no. 248, pp. 73-76, 1990.